A CLIMATOLOGY OF PACIFIC ITCZ CHARACTERISTICS FROM AN AUTOMATED, OBJECTIVE ALGORITHM

A Thesis

by

KYLE ROBERT WODZICKI

Submitted to the Office of Graduate and Professional Studies of
Texas A&M University
in partial fulfillment of the requirements for the degree of

MASTER OF SCIENCE

Chair of Committee,	Anita D. Rapp
Committee Members,	Kenneth P. Bowman
	Steven M. Quiring
Head of Department,	Ping Yang

December 2015

Major Subject: Atmospheric Sciences

ABSTRACT

The Intertropical Convergence Zone (ITCZ) is a main driver of the Hadley circulation and a large component of the hydrologic cycle. With recent studies indicating changes in the width and strength of the Hadley circulation it is possible that changes in ITCZ characteristics may be related to these changes. The goal of this study is to identify changes in the characteristics of the ITCZ that have occurred over the past three decades. The automated ITCZ identification algorithm of Berry and Reeder is modified and applied to ECMWF Reanalysis Interim (ERA-Interim) variables and the ITCZ latitude at each longitude is used as a starting point to objectively characterize ITCZ width and intensity. TRMM Microwave Imager (TMI) and Global Precipitation Climatology Project (GPCP) rain rates (RRs) are used to examine the 15- and 36-year climatologies, respectively, of northern and southern ITCZ convection boundaries, ITCZ width, and precipitation intensity within the center and across the entire ITCZ extent in the tropical Pacific. The climatological location of the ITCZ was found near 8°N, consistent with previous studies, with a preferred southern boundary location of 4°S. The northern ITCZ boundary did not exhibit a preferred boundary with locations between $7° - 15°$N having similar frequencies of occurrence. The northern and southern extents of the ITCZ were symmetric in the central Pacific and asymmetric in the east Pacific. Long-term trends in the width and ITCZ precipitation intensity showed narrowing and intensifying trends significant at the 95% confidence level. Separation of characteristics by season and location (i.e., central and eastern Pacific) revealed negative trends in the width of the ITCZ in both domains, with trends in the east Pacific weaker than those in the central Pacific. Trends in precipitation intensity near the center of the ITCZ indicate even

more precipitation intensification than over the whole ITCZ, with slightly stronger trends in the central Pacific than in the east Pacific. Interestingly, regression of monthly mean ITCZ width and intensity are positively correlated, indicating heavier mean RR when the ITCZ is wider. These findings show that while the mean center location of the ITCZ has not changed significantly over the past three decades, the ITCZ has narrowed and precipitation has intensified; however, the different mechanisms that drive relationships between ITCZ width and precipitation intensity at different timescales is still unclear.

DEDICATION

To my fiancée and my parents for their love and support

ACKNOWLEDGEMENTS

I would like to thank my advisor, Dr. Anita Rapp, for not only providing me the opportunity to attend graduate school, but for helping me to become a better scientist and researcher. Without her flexibility and kindness I would never have been able to complete this thesis and for that I am forever grateful. I would also like to thank my committee members, Dr. Kenneth Bowman and Dr. Steven Quiring, for taking time to provide feedback and ideas to improve my work, with an extra thank you to Dr. Bowman for his help with IDL. I must also thank Jack and Chris for their help debugging code, and to Chris, Keith, Hannah, and all my colleagues who have made my time at Texas A&M enjoyable.

Lastly, I must thank my parents for all their support throughout my life and wish to thank my fiancée Tara for her encouragement.

NOMENCLATURE

AGCM	Atmospheric general circulation model
AMIP	Atmospheric Model Intercomparison Project
AR5	Fifth Assessment Report
CAM	Community Atmospheric Model
CAMS	Climate Assessment and Monitoring System
CCM3	Community Climate Model, version 3
CERES	Clouds and Earth's Radiant Energy System
CMIP5	Coupled Model Intercomparison Project Phase 5
ECMWF	European Centre for Medium-Range Weather Forecasts
ENSO	El Niño Southern Oscillation
ERA-40	ECMWF 40-year Reanalysis
ERA-Interim	ECMWF Reanalysis Interim
GCM	General circulation model
GHCN	Global Historical Climate Network
GPCC	Global Precipitation Climatology Centre
GPCP	Global Precipitation Climatology Project
GPROF	Goddard Profiling Algorithm

HRC	Highly reflective cloud
IPCC	Intergovernmental Panel on Climate Change
ITCZ	Intertropical Convergence Zone
LIS	Lightning Imaging System
MCS	Mesoscale convective system
MEI	Multivariate ENSO Index
MERRA	Modern Era Retrospective-Analysis for Research
MRF	Markov random field
NCAR	National Center for Atmospheric Research
OLR	Outgoing longwave radiation
PF	Precipitation feature
PR	Precipitation radar
QTCM	Quasi-equilibrium tropical circulation model
RPF	Radar precipitation feature
RR	Rain rate
RSS	Remote Sensing Systems
SPCZ	South Pacific Convergence Zone
SSM/I	Special Sensor Microwave/Imager
SST	Sea surface temperature

TIROS	Television and Infrared Observation Satellite
TMI	TRMM Microwave Imager
TOVS	TIROS Operational Vertical Sounder
TPW	Total precipitable water
TRMM	Tropical Rainfall Measuring Mission
UMORA	Unified Microwave Ocean Retrieval Algorithm
VIRS	Visible and Infrared Radiometer System

TABLE OF CONTENTS

Page

LIST OF FIGURES

FIGURE Page

LIST OF TABLES

TABLE Page

1. INTRODUCTION

The Intertropical Convergence Zone (ITCZ) is arguably the most important feature of the tropical atmosphere. This semi-permanent feature is located within the equatorial trough created by the convergence of northeasterly and southeasterly trade winds (Figure 1.1) and is characterized by a broad region of ascent, enhanced cloudiness (Bjerknes et al. 1969; Hubert et al. 1969; Gruber 1972), and precipitation (Estoque and Douglas 1978; Dorman and Bourke 1979; Frank 1983). The enhanced precipitation observed in the ITCZ is shown for the Pacific basin using mean Global Precipitation Climatology Project (GPCP) rain rates (RRs), over the period January 1979 to December 2014, in Figure 1.2a. RRs greater than 8 mm day^{-1} are oriented in a zonal band that spans the entire Pacific Ocean between 0°-15°N and signify the ITCZ. A secondary area of increased precipitation, the South Pacific Convergence Zone (SPCZ), is located between roughly 0°S;150°E and 20°S;150°W. Regions of low precipitation in the subtropics of both hemispheres (15°-30°N and 15°-30°S) are indicative of subsidence in these regions associated with the downward branch of the Hadley circulation. These regions of reduced precipitation are more prominent in the east Pacific due to the combination of subsidence and lower sea surface temperatures (SSTs). From Figure 1.2 the climatological location of the ITCZ in the Pacific appears to be near $\sim$ 8°N, which has been verified by many studies using satellite data (e.g., Gruber 1972; Mitchell and Wallace 1992; Waliser and Gautier 1993) and numerical models (e.g., Pike 1971; Holton et al. 1971; Charney 1971; Waliser and Somerville 1994).

On shorter time scales, such as daily or weekly, the ITCZ may not appear as a continuous line of convection, but rather many isolated convective clusters as in

Figure 1.2b. It is also possible that the ITCZ may not be identifiable on a given day (Holton et al. 1971; Frank 1983; Wang and Magnusdottir 2006). Because of this variability and the large impacts the ITCZ has on atmospheric circulations and the hydrologic cycle, it has been the focus of numerous studies. Many early studies examined the structure of the ITCZ (i.e., profiles of convergence and heating, rainfall, and cloud cover) on the synoptic scale using data from field campaigns (e.g., Estoque and Douglas 1978; Frank 1983), while others studied the role the ITCZ plays in atmospheric circulations. These studies indicated that convection within the ITCZ is the main driver of the Hadley circulation (Fletcher 1945; Riehl and Malkus 1958; Asnani 1968).

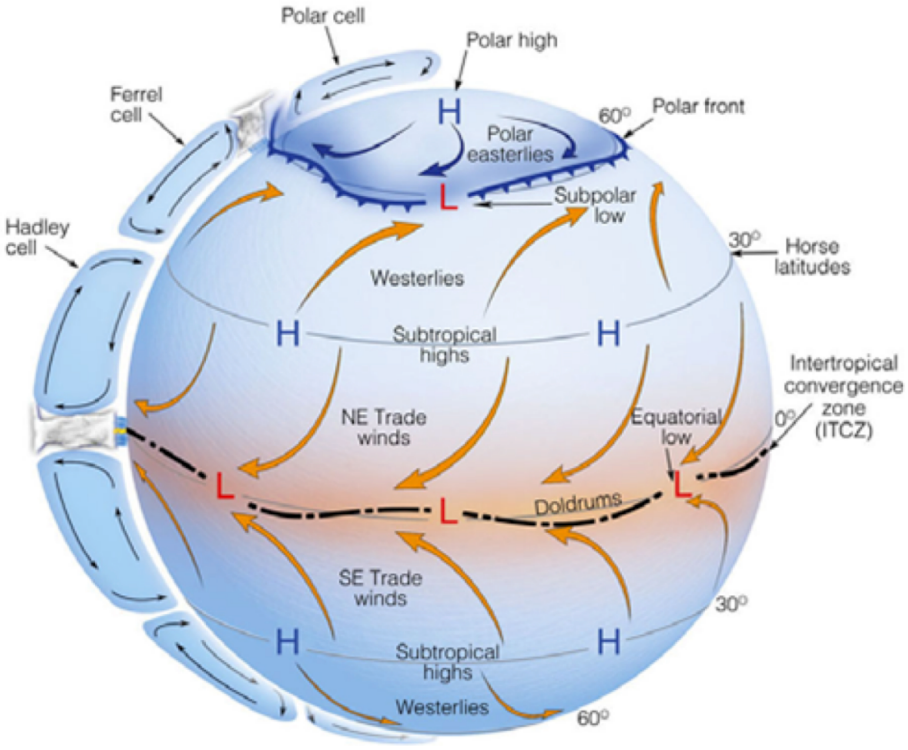

Figure 1.1: The idealized wind and surface-pressure distribution over a uniformly water-covered rotating earth. Source: Ahrens (2007).

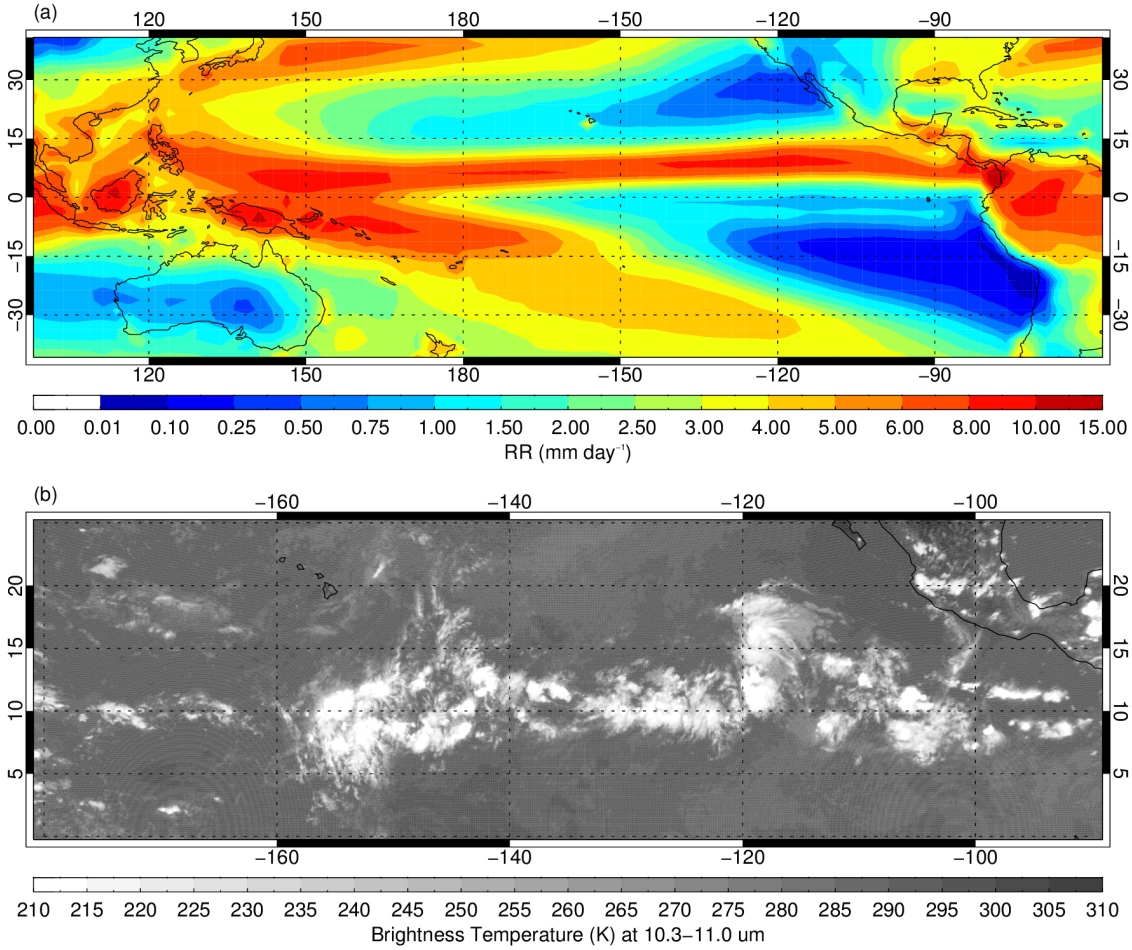

Figure 1.2: (a) Climatological mean RR from the GPCP for the time period January 1979 to December 2014. (b) Infrared brightness temperature for 2100 UTC 19 August 2000 showing the discontiguous nature of the ITCZ on daily time scales.

The Hadley circulation is responsible for the redistribution of heat from the tropics to the mid latitudes. The circulation consists of a rising branch, constituted by the ITCZ, and a descending branch located between 20°-30° latitude in both hemispheres (Figure 1.1). At upper levels, air moves poleward transporting heat to higher latitudes with return flow at lower levels (Webster 2004). The ascending and descending branches of the circulation also define the wettest and driest regions of

the world, with the heaviest rainfalls located in the ascending branch (i.e., the ITCZ identified in Figure 1.2a) and world's deserts located in the dry descending branches (i.e., the subtropical precipitation minima identified in Figure 1.2a; Webster 2004; Lu et al. 2007; Seidel et al. 2008; Stachnik and Schumacher 2011; Nguyen et al. 2013). Because of the large influence the Hadley circulation has on the hydrologic cycle, changes in the circulation can have major impacts on large regions of the globe. One example is a shift in the ascending branch of the Hadley circulation to the north or south, which would change rainfall patterns and negatively impact agriculture. Thus, it is important to determine if the Hadley circulation is changing and where changes in the circulation originate.

In recent years, much work has been done to determine if the Hadley circulation has been changing in a warming climate. General circulation models (GCMs) from the Intergovernmental Panel on Climate Change (IPCC) Fifth Assessment Report (AR5) exhibited possible changes such as deepening and narrowing of ITCZ convection, broadening of the Hadley circulation, and a reduction in subtropical low clouds (Figure 1.3). While some of the changes exhibit robust positive climate feedbacks (red arrows), the contributions of other feedbacks are uncertain (red arrows). The reduction in subtropical low clouds shown in Figure 1.3 may be due to increased subsidence associated with increased overturning in the Hadley circulation; however, because a strengthening of the circulation is not discussed, it is likely that GCMs still exhibit variability in changes of circulation strength. This reasoning aligns with the results of Mitas and Clement (2006) who showed a large amount of variability in changes of Hadley circulation strength between GCMs. A narrowing of the ITCZ is also shown in Figure 1.3, which may be due to a remote feedback outlined by Neggers et al. (2007). Their work suggests that a reduction of subtropical moisture ultimately leads to changes in the convective intensity and extent of the ITCZ. This

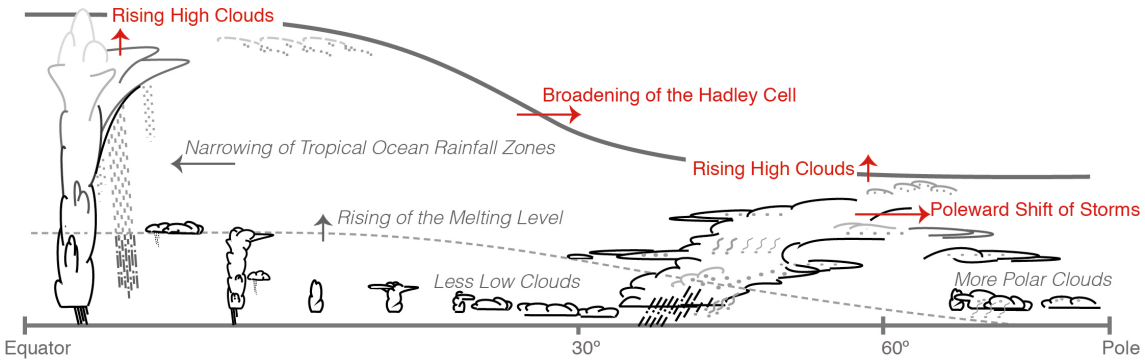

Figure 1.3: Robust cloud responses to greenhouse warming (those simulated by most models and possessing some kind of independent support or understanding). The tropopause and melting level are shown by the thick solid and thin grey dashed lines, respectively. Changes anticipated in a warmer climate are shown by arrows, with red colour indicating those making a robust positive feedback contribution and grey indicating those where the feedback contribution is small and/or highly uncertain. No robust mechanisms contribute negative feedback. Changes include rising high cloud tops and melting level, and increased polar cloud cover and/or optical thickness (high confidence); broadening of the Hadley Cell and/or poleward migration of storm tracks, and narrowing of rainfall zones such as the Intertropical Convergence Zone (medium confidence); and reduced low-cloud amount and/or optical thickness (low confidence). Confidence assessments are based on degree of GCM consensus, strength of independent lines of evidence from observations or process models and degree of basic understanding. Source: Boucher et al. (2013).

is discussed in more detail in Section 4 of this study.

Although the aforementioned ITCZ studies determined many of the ITCZ's traits, there has been less work quantifying the variability in extent and intensity of convective feature characteristics of the ITCZ and how these traits interact and influence one another. One example of a possible interaction is how the intensity of convection in the ITCZ changes when the ITCZ is anomalously narrow or wide. As a result, changes within the ITCZ (i.e., location, width, and precipitation intensity) and their relationship to changes in the large scale circulation and the hydrologic cycle are not completely understood. This is illustrated through results of idealized model-

ing studies, which produced either little or significant changes in Hadley circulation strength when the location of heating (i.e., the ITCZ) was displaced from the equator (Lindzen and Hou 1988; Hack et al. 1989; Walker and Schneider 2005). However, Hu et al. (2007) found large changes in the Hadley cell half-width coincided with changes in the location of the ITCZ based on reanalysis and observational RR data. Kumar et al. (2004) attributed a strengthening of the ascent region of the Hadley circulation since 1950 observed in two atmospheric general circulation models (AGCMs) to increases in RRs, which were linked to increases in vertical motion and latent heat release. These findings suggest a link between observed changes in the Hadley circulation (Mitas and Clement 2005; Hu et al. 2011; Stachnik and Schumacher 2011; Nguyen et al. 2013) and changes in ITCZ characteristics.

In recent years, many studies have been performed on apparent changes in the strength of the Hadley circulation and expansion of the tropics. Mitas and Clement (2005) showed that two of three reanalyses studied exhibited a strengthening of the Hadley circulation in boreal winter, while the third reanalysis and rawinsonde data showed no significant trend. An ensemble of Community Atmospheric Model (CAM) runs produced a positive trend, albeit weaker than in reanalyses, in the strength of the circulation when SSTs were increased. Hu et al. (2011) also found evidence of Hadley circulation expansion in multiple independent observational datasets and an ensemble of GCMs; however, there was a large amount of variation in the magnitude of expansion between the data sets.

An exhaustive study of Hadley circulation changes in reanalyses was performed by Nguyen et al. (2013). Their results showed a qualitative agreement in intensity, width, and extent of the Hadley circulation between all the reanalyses; however, there were some significant differences in the trends and the strength of the Hadley circulation varied widely. These variations were attributed to differences in data

assimilation and model physics between reanalyses and has been supported by other similar studies (Mitas and Clement 2005, 2006; Stachnik and Schumacher 2011).

While evidence of expansion and intensification of the Hadley circulation has been observed in reanalysis and observational datasets, these changes are much weaker or nonexistent in GCMs. Mitas and Clement (2006) studied nearly 100 simulations from 34 GCMs and found that the majority showed decreases or little change in the strength of the circulation. The discrepancy between trends in observational and reanalysis data and the lack of trends in GCMs has been attributed to differences in model parameterizations (Mitas and Clement 2006; Hu and Fu 2007; Hu et al. 2011). These differences have a much larger impact on GCM output than on reanalyses, as GCMs are not heavily constrained by observations.

Many of the aforementioned studies used a zonal-mean meridional stream function to quantify the strength of the overturning in the Hadley circulation (Mitas and Clement 2005; Hu and Fu 2007; Stachnik and Schumacher 2011; Nguyen et al. 2013); however, this is not necessarily a direct measure of characteristics of the ITCZ that constitutes the ascending branch. Therefore, the lack of or weak changes in the Hadley circulation in GCMs may be partially due to errors in the representation of the ITCZ (Kumar et al. 2004; Quan et al. 2004), which cannot be identified through the stream function alone. An example of a common error in the representation of the ITCZ is the so-called double ITCZ problem. In an attempt to mitigate this problem, Oueslati and Bellon (2013) studied the impact that different magnitudes of entrainment had on model precipitation from Atmospheric Model Intercomparison Project (AMIP) and Coupled Model Intercomparison Project Phase 5 (CMIP5) simulations. They found that increased entrainment reduced the double ITCZ problem, however, it also increased precipitation along the ITCZ. Using a modified version of the Zhang-McFarlane scheme (Zhang and McFarlane 1995) in the National Center

for Atmospheric Research (NCAR) Community Climate Model, version 3 (CCM3), Zhang and Mu (2005) found large improvements in the distribution of precipitation produced by the model, with no RRs above 3 mm day^{-1} before the modification and RRs closely matching observations from the Tropical Rainfall Measuring Mission (TRMM) after modification. Although some regions saw improvements in RRs (i.e., the Saudi Arabian peninsula and western North Pacific monsoon region), some regions saw reductions (i.e., the eastern Pacific ITCZ). These results are in contrast to the increase in ITCZ precipitation from Oueslati and Bellon (2013) and indicates the large amount of uncertainty introduced through parameterizations. Along with errors in precipitation intensity in GCMs, errors in the migration of the ITCZ have also been linked to parameterization errors (Wu et al. 2003). To determine what types of errors are present in model representations of the ITCZ and ultimately, what aspect of the model is responsible for the errors, a long-term, observationally-based climatology of ITCZ characteristics is needed to compare to ITCZs produced by models. Thus, this study aims to create a more comprehensive and objective climatology of the characteristics of the ITCZ and will examine the long-term variability and co-variability in ITCZ characteristics.

In the past few decades there have been many studies involving identification of the ITCZ's location (e.g., Waliser and Gautier 1993; Bain et al. 2011) and characterization of general precipitation features (PFs) and rainfall in the tropics (e.g., Nesbitt et al. 2000; Lau and Wu 2007, 2011). Waliser and Gautier (1993) used the highly reflective cloud (HRC) dataset, created through subjective analysis of visible and infrared satellite imagery (Garcia 1985), to study the location of convection in the ITCZ. In their work, the number of days in a given month where a HRC was present in a pixel was used as a measure of convective intensity. Although the HRC was found to represent the presence of deep convection well, it is not a direct measure of

precipitation or convective intensity. Although Waliser and Gautier (1993) provided invaluable results about the preferred latitude, seasonal migration, and anomalies in the location of the ITCZ, analyses were confined to the HRC data period (1971-1987) and the identification method was not objective.

Bain et al. (2011) used a different approach to identify the ITCZ. They used three satellite observations (i.e., infrared brightness temperature, visible reflectance, and total precipitable water (TPW)) in a Markov random field (MRF) statistical model to create a binary ITCZ presence for each grid point. Two identifications were performed; one with all three datasets for a time period of 1995-2008, and a second with only the infrared data for a time period of 1980-2009. The MRF model was trained with manual ITCZ identifications from three different meteorologists for every day of August 2000 with the model producing binary ITCZ identifications at 0.5° resolution at three-hour time steps. Seasonal and interannual variability of the ITCZ location was similar to the results of Waliser and Gautier (1993). They also found no significant trend in the location of the ITCZ from 1980 to 2009. A link between ITCZ width and El Niño Southern Oscillation (ENSO) was identified with a wider (narrower) ITCZ present during El Niño (La Niña).

Although this method of ITCZ identification does allow for a longer time series analysis because of the long history infrared satellite data, it has limitations. The authors noted that identifications in the central Pacific with only infrared data suffered due to the difficulty identifying warmer clouds in infrared frequencies. Another limitation of this approach is that the model must be trained sufficiently for the results to be meaningful. Therefore, a more objective approach to identify the location of the ITCZ is desired. Berry and Reeder (2014) applied an objective, automated ITCZ identification algorithm to daily dynamic and thermodynamic fields derived from European Centre for Medium-Range Weather Forecasts (ECMWF) Reanalysis

Interim (ERA-Interim) variables. The derived fields were used as masks to signify whether the ITCZ could or could not be present in a given region at daily time scales. An adaptation of their algorithm to monthly time scales is used as a starting point for this study. Along with identifying the center location of the ITCZ, it is important to determine the extent and intensity of precipitation and convection within the ITCZ as changes in the concentration of latent heating can affect the Hadley circulation (Lindzen and Hou 1988; Hou and Lindzen 1992; Dodd and James 1997). Although the heating profile of the atmosphere is the main driver of the Hadley circulation (Tao et al. 2006), the level at which maximum heating occurs is also extremely important as it is collocated with the maximum vertical velocity (Webster 2004).

Many different satellite metrics have been used to determine the intensity of convection. Nesbitt et al. (2000) used six separate metrics based on radar or radiometer observations to study convection in the tropics using the TRMM satellite. These metrics included the area of convective systems, minimum polarization corrected temperature, maximum height of the 30-dBZ echo, maximum reflectivity at 6-km, lightning frequency, and volumetric rainfall. These and similar metrics have been shown to represent convective characteristics quite well; however, the present study will use RR intensity so that the intensity of the ITCZ can be determined over the entire 36-year GPCP period. RR intensity has been linked to many of the aforementioned intensity metrics with a strong correlation between the height of the 30-dBZ echo and rainfall rate (DeMott and Rutledge 1998) and links between rainfall rate and maximum storm height and updraft velocity (Cheng and Houze Jr. 1979; Short et al. 1997).

In an effort to extend results of the aforementioned studies and provide a comprehensive assessment of the co-variability in ITCZ characteristics, this study attempts to objectively identify the central location of the ITCZ, its northern and southern

extent, and the intensity of ITCZ precipitation over the Pacific Ocean on a monthly time scale. The ITCZ center location is identified by modifying the method outlined by Berry and Reeder (2014) for application to monthly mean reanalysis data. This center location is then used as the starting point to locate boundaries of ITCZ convection with monthly mean TRMM Microwave Imager (TMI) RRs. TMI RRs near the center of the ITCZ, where the most intense convection should be located, and over the entire ITCZ are used to capture ITCZ precipitation intensity. These methods are then modified and applied to GPCP RRs (Adler et al. 2003; Huffman et al. 2009), which allows an extension of the ITCZ characteristics climatology from the 15 years of TRMM data to 36 years.

2. DATA AND METHODS

The ITCZ characterization algorithm uses the ERA-Interim (Dee et al. 2011) for ITCZ center location identification, and Remote Sensing Systems (RSS) version 4 TMI RR data (Wentz 1997; Hilburn and Wentz 2008), for location of ITCZ boundaries. The sensitivity of identifications to the reanalysis system is also tested by applying the algorithm to Modern Era Retrospective-Analysis for Research (MERRA, Rienecker et al. 2011). Upon completion of the full algorithm, it is run using ERA-Interim variables and TMI RRs, as well as GPCP (Adler et al. 2003; Huffman et al. 2009) RRs to determined the sensitivity of boundary identifications to the RR dataset. The use of GPCP RRs is also required to extend the ITCZ climatology to 36 years, more than double the 15 years of TMI RRs available. The final dataset analyzed is from the TRMM PF database (Nesbitt et al. 2000; Liu 2007; Liu et al. 2008), which will be used in a preliminary study of changes in the convective characteristics of the ITCZ.

For the identification of the ITCZ all data are located in a domain of 40°S - 40°N; 100°E - 60°W, with ITCZ analysis restricted to 160°E-100°W to minimize false ITCZ identifications in the warm pool region of the west Pacific and near the coast of the Americas in the east Pacific. These boundaries also correspond with the central and east Pacific domains used by Waliser and Gautier (1993).

The intensity of precipitation in the ITCZ is determined using monthly mean RRs from the TMI and GPCP datasets discussed above. All pixels from each dataset that are located within the northern and southern boundaries of the ITCZ in a given month are identified as precipitation rates for the ITCZ. These pixels are then averaged to obtain a monthly mean ITCZ RR, which is used to signify the intensity

of precipitation in a given month. TMI and GPCP pixels located near the center of the ITCZ are also identified and averaged in order to measure the intensity of precipitation for the most convective area of the ITCZ.

2.1 Reanalysis Data

The ITCZ location method used in this study is adapted from Berry and Reeder (2014) and requires variables that are only available from reanalyses or GCMs. The variables from the ERA-Interim used for the ITCZ location are shown in Table 2.1. The ERA-Interim was chosen because Berry and Reeder (2014) also used the ERA-Interim in their work, however the results are also compared to MERRA.

Table 2.1: Variables used in the location of the ITCZ. All pressure levels between 1000 and 850 hPa were used in the layer means.

Variable	Levels Required (hPa)	Native Resolution	Resolution Used	Time Step
u-component of wind	1000-850	$\sim 0.7^\circ \times 0.7^\circ$	$1.5^\circ \times 1.5^\circ$	6 hourly
v-component of wind	1000-850	$\sim 0.7^\circ \times 0.7^\circ$	$1.5^\circ \times 1.5^\circ$	6 hourly
Temperature	850	$\sim 0.7^\circ \times 0.7^\circ$	$1.5^\circ \times 1.5^\circ$	6 hourly
Relative Humidity	850	$\sim 0.7^\circ \times 0.7^\circ$	$1.5^\circ \times 1.5^\circ$	6 hourly

The ERA-Interim was developed as a replacement for the previous ECMWF reanalysis system, the ECMWF 40-year Reanalysis (ERA-40), and to act as a bridge to future reanalyses. The main goal of the project was to improve the assimilation of data over the ERA-40 to reduce model errors, such as the representation of the hydrologic cycle (Dee et al. 2011). While marked improvements over ERA-40 to fields such as tropical winds (Bechtold et al. 2004), divergent winds, and the moisture budget (Berrisford et al. 2011) were achieved with the ERA-Interim, errors still exist

in the system. For example, Berrisford et al. (2011) noted extended periods where differences between precipitation and evaporation were either primarily negative or positive, illustrating that errors in the hydrologic cycle are still present. However, the ITCZ identification method thresholds used in this study can be tuned to compensate for any errors that may influence identifications.

2.2 Rain Rate Datasets

This study requires RR data to determine the location of ITCZ convective boundaries. One of the RR datasets used is derived from the TMI onboard the TRMM satellite. Launched on 27 November 1997, TRMM was designed to study rainfall and energy exchanges in the tropics and subtropics to improve the understanding of the hydrologic cycle and GCMs (Simpson et al. 1988; Kummerow et al. 1998). Orbiting the earth at a 35° inclination in a non-sunsynchronous orbit, TRMM completed roughly 16 orbits per day. The initial altitude of TRMM was 350 km until 22 August 2001 when TRMM was boosted to an altitude of 402 km to extend the life of the satellite. This boost allowed the TRMM mission to continue another 14 years, with the mission ending on 15 April 2015. Five instruments were onboard the satellite: TRMM Microwave Imager (TMI), precipitation radar (PR), Visible and Infrared Radiometer System (VIRS), Clouds and Earth's Radiant Energy System (CERES), and Lightning Imaging System (LIS). Scan geometries for the PR, TMI, and VIRS instruments are shown in Figure 2.1. Data from two instruments, the TMI and the PR, will be used in this study, with retrievals from both of these instruments affected by the orbit altitude boost.

Shin and Chiu (2008) found that the orbital altitude boost caused a reduction in the 3A11 TMI monthly $5° \times 5°$ RR product; however, this was mitigated through adjustments to the beam-filling correction and brightness temperature estimates used

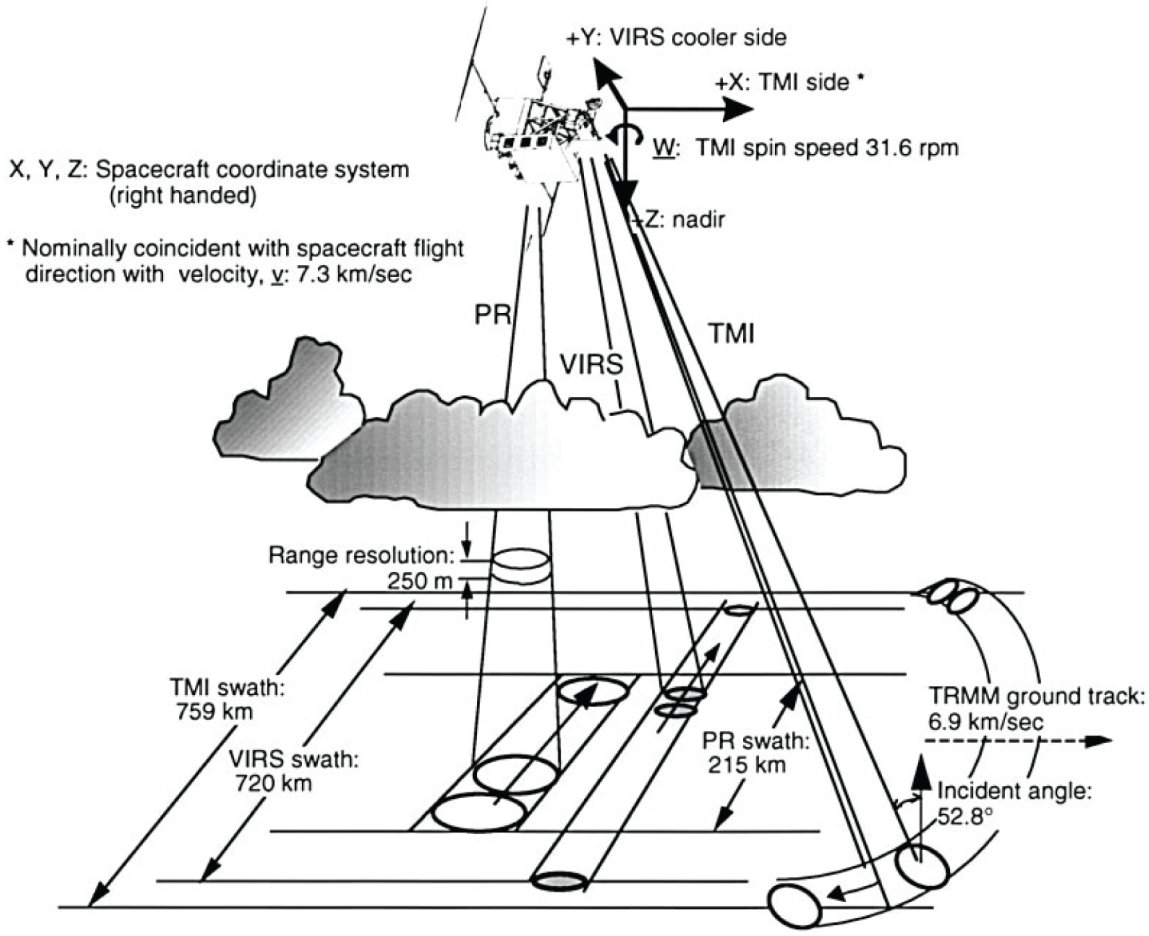

Figure 2.1: Scan geometry of TMI, PR, and VIRS onboard the TRMM satellite. Source: Kummerow et al. (1998).

in the RRs estimation algorithm. A similar study of over ocean only RRs from the TMI 2A12 algorithm was performed by DeMoss and Bowman (2007). They found that 2A12 RRs were biased $\sim$ 12% low pre-boost and $\sim$ 1% low postboost relative to buoy rain gauges. This orbit altitude boost effect is most likely present in the RSS TMI RR product used in this study as Hilburn and Wentz (2008) showed that differences between their product and TMI 2A12 RRs remained steady for the pre- and postboost period. Although the impacts of these pre- and postboost

effects are important when interpreting results, the use of TMI RRs is limited to the development of the ITCZ characterization algorithm. However, any influence of the altitude boost during time series analysis will be noted and corrected if it is determined to be impacting the results of the study.

The TMI is a passive microwave radiometer with nine-channels and was modeled after the Special Sensor Microwave/Imager (SSM/I) (Kummerow et al. 1998). Although the instruments are very similar, two changes were made for the TMI: horizontal and vertically polarized 10.7-GHz channels were added and the water vapor channel was shifted from 22.235 to 21.3-GHz to avoid saturation in the tropical orbit. The antenna of the TMI rotates about a nadir axis with a 52.8° incident angle at the earth's surface; however, only 130° of the rotation are used for sampling of the atmosphere creating a swath width of roughly 760 km pre-boost and 878 km post-boost (Kummerow et al. 1998).

The RSS TMI RRs used in this study were retrieved using the Unified Microwave Ocean Retrieval Algorithm (UMORA; Wentz and Spencer 1998; Hilburn and Wentz 2008). UMORA uses brightness temperatures (T_B) from the 19- and 37-GHz TMI channels to estimate RR over oceans through an empirically based formula. The algorithm also accounts for the three parameters that affect passive microwave RR estimates (i.e., beam-filling, cloud-rain partitioning, and effective rain layer thickness) by separating and tuning the corrections for each effect to obtain the most accurate RR retrievals possible. RR retrievals from the 19- and 37-GHz channels are then blended to improve the estimations. The final TMI RR retrievals are available as $0.25° \times 0.25°$ gridded binary files at daily, 3-day, weekly, and monthly time scales from RSS (http://www.remss.com).

Passive microwave RRs do suffer from errors at low RRs (Kummerow et al. 1996); however, Bauer et al. (2002) showed that spatial averaging of RR estimations greatly

improved the estimations. Hilburn and Wentz (2008) showed that TMI RR estimations from the UMORA algorithm matched well to the Goddard Profiling Algorithm (GPROF) used in the standard 2A12 RR estimations, except when comparing instantaneous retrievals at the pixel level. Because this study is using monthly mean RRs from UMORA, with the data retrieved at the 37 GHz spatial resolution (16×9 km) and gridded to $0.25^\circ \times 0.25^\circ$, both spatial and temporal averaging is included in the dataset, which should greatly reduce estimation errors.

A second RR dataset, the GPCP (Adler et al. 2003; Huffman et al. 2009), is also used as the GPCP dataset extends from 1979 to the present; a period more than twice the length of TRMM observations. GPCP combines RR data from a number of satellite-based estimates and rain gauge data to use the strengths of each dataset in an effort to produce the most accurate global precipitation data possible. The satellite retrievals used in the GPCP include SSM/I, geostationary infrared, Television and Infrared Observation Satellite (TIROS) Operational Vertical Sounder (TOVS), and low-Earth orbit outgoing longwave radiation (OLR), with the rain gauge data from the Global Precipitation Climatology Centre (GPCC) and combined Global Historical Climate Network (GHCN) and Climate Assessment and Monitoring System (CAMS). To a degree, the GPCP reached its goal of creating a highly accurate global RR dataset; however, Adler et al. (2003) notes that the GPCP does have limitations. One major limitation is the lack of SSM/I data in the pre-1987 period, which creates inhomogeneities in the time series, while climatological mean RRs at mid and high latitudes over the ocean are dependent on TOVS or OLR data. The latter of these limitations should not influence the results of the current study as RRs outside of the tropics will not be considered; however, the former will have to be considered in the final analysis. The GPCP data are available as $2.5^\circ \times 2.5^\circ$ gridded binary files at monthly time scales (http://precip.gsfc.nasa.gov).

2.3 Precipitation Feature Database

The PR is the first space based rain radar and was included in the TRMM sensor packaged to obtain the three-dimensional structure of systems and for combined retrievals with the TMI and VIRS. Operating at 13.6 GHz, the PR views the earth at nadir with a 215 km swath width and 250 m vertical resolution (Kummerow et al. 1996). Pre- and postboost footprint sizes of the PR are 4.3 and 5 km, respectively. This boost not only affected TMI retrievals, as discussed in Section 2.2, it also affected the PR. A study of the impacts the orbit altitude boost had on PR reflectivity distributions performed by Short and Nakamura (2010) found that reflectivities between 20-34 dBZ increased 2-3% in the 3A25 product postboost. Although this change in reflectivity distributions will impact some of the convective intensity metrics studied in the current work, the study of PR-derived convective parameters is confined to the postboost period to minimize biases.

For the TRMM time period, the TRMM PF database (Nesbitt et al. 2000; Liu 2007; Liu et al. 2008) will be used for a preliminary analysis to better quantify changes in the characteristics of convection in the ITCZ. The TRMM PF database was developed to allow for faster, more efficient analysis of TRMM data. This is accomplished through the grouping of contiguous TMI, PR, or VIRS pixels (based on the definition used) and providing various commonly used parameters (e.g., number of pixels in the feature, minimum brightness temperature, maximum height, etc.) to study feature characteristics. There are many different PF definitions in the database, with the radar precipitation feature (RPF) definition used for this study. All TRMM PR data is derived from RPFs within the PF database. RPFs are defined as any pixel or contiguous group of pixels with rainfall from the PR 2A25 algorithm (Iguchi et al. 2000) greater than 0 mm hr^{-1} (Liu et al. 2008).

2.4 Method for ITCZ Identification

To identify the center location of the ITCZ, a method similar to Berry and Reeder (2014) is applied. Although Berry and Reeder (2014) used a seven-day running mean for ITCZ location analysis on a daily time scale, a monthly mean analysis is sufficient for the long-term climatology developed here. Therefore, this method is modified and applied to monthly means of the 6-hourly ERA-Interim fields to identify the monthly mean ITCZ location at $1.5° \times 1.5°$ resolution across the Pacific. For comparison to the daily data example in Berry and Reeder (2014, their Figure 2), each step of this method is recreated for the August 2004 monthly mean data in Figure 2.3. A flow chart of the ITCZ identification method is shown in Figure 2.2.

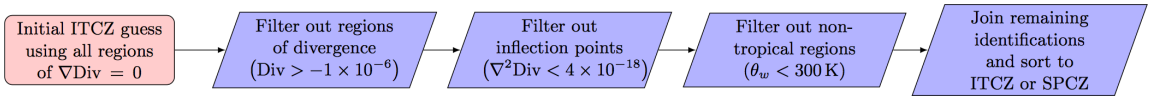

Figure 2.2: Outline of the ITCZ identification method from Berry and Reeder (2014).

The first step of the ITCZ identification method requires calculating the 1000-850 hPa layer mean divergence from five-point smoothed u- and v-wind components. Berry and Reeder (2014) chose a layer mean divergence to allow for the use of the method over both land and sea, while the time mean was used to reduce the influence of synoptic-scale events on the ITCZ location. It is clear from the monthly layer mean divergence in Figure 2.3a (color) that the ITCZ is most likely located in the zonal band of convergence between $0 - 15°$N. From this data, the gradient of divergence is calculated and locations where the gradient of divergence equals zero, representing divergence minima and maxima, are taken as an initial guess for the ITCZ location. The black lines in Figure 2.3a indicate all locations where the gradient of divergence

equals zero. Although this does place a possible ITCZ directly in the center of the zonal band of convergence mentioned earlier, there are many locations (i.e., lines south of the equator and north of 15°N) that are most likely not representative of the location of the ITCZ.

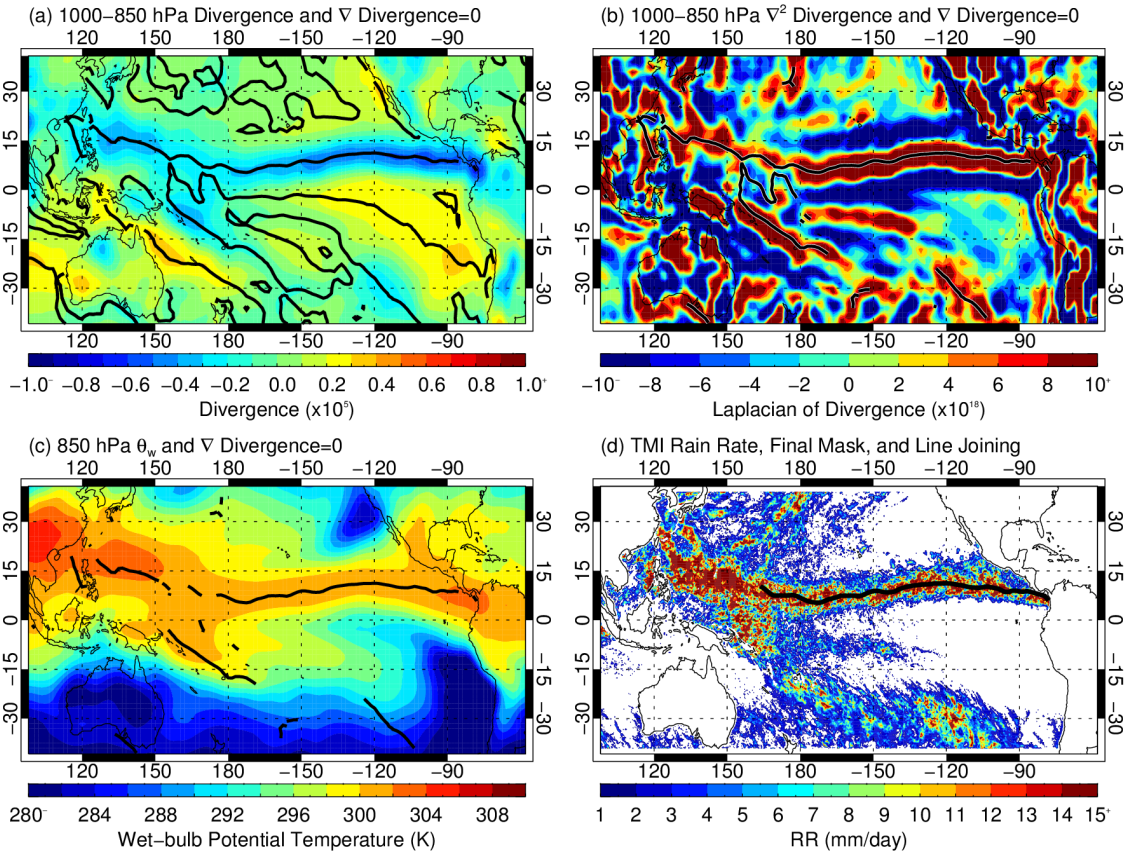

Figure 2.3: Reproduction of the ITCZ identification method outlined by Berry and Reeder (2014) (similar to their Figure 2), for August 2004. (a) Divergence (color) and gradient of divergence equal to zero (line); (b) Laplacian of divergence (color) and gradient of divergence equal to zero with divergence mask (line); (c) θ_w (color) and gradient of divergence equal to zero with divergence and Laplacian of divergence masks (line); (d) TMI RR (color) and gradient of divergence equal to zero with divergence, Laplacian of divergence, and θ_w masks and line joining.

To remove these misidentified locations, the monthly layer mean divergence is used to mask the initial ITCZ locations, with all ITCZ locations in areas where the divergence is above a divergence threshold (-1×10^{-6} s^{-1}) removed. Application of this mask to the initial ITCZ identifications is shown in Figure 2.3b (black lines), where almost all of the misidentifications located in the southeast Pacific and north of 15°N are removed. The second mask uses the Laplacian of the monthly layer mean divergence to remove inflection points that can cause the gradient of divergence to equal zero at places other than divergence minima and maxima. Because the Laplacian of divergence is the divergence of the gradient of divergence, locations of maximum Laplacian of divergence will be co-located with absolute divergence minima. Figure 2.3b (color) shows the Laplacian of divergence. In this case, almost all of the possible ITCZ locations remaining fall within a Laplacian of divergence maximum (red) with only a few locations in the warm pool region of the Pacific falling in Laplacian of divergence minima (blue). Application of the Laplacian of divergence mask is shown in Figure 2.3c, with all possible ITCZ locations below the Laplacian of divergence threshold (4×10^{-18} m^{-2} s^{-1}) removed.

The final mask applied is the monthly mean wet bulb potential temperature (θ_w) at 850 hPa (Figure 2.3c color), which is a thermodynamic parameter used to distinguish the tropics from the extratropics. It is clear in Figure 2.3c that the majority of the possible ITCZ locations lie within the tropics (i.e., regions where $\theta_w \geq 297$ K) with the rest of the ITCZ locations falling outside the tropics (i.e., regions where $\theta_w < 297$ K). Application of the θ_w mask removes the misidentifications in the extratropics, leaving only valid ITCZ identifications.

Application of the Berry and Reeder (2014) ITCZ identification method to monthly time scales required some modifications to the masking thresholds. The Laplacian of divergence and θ_w thresholds used by Berry and Reeder (2014) for daily analysis

resulted in the removal of valid ITCZ identifications for some cases based on visual inspection of TMI RR imagery. After testing, the Laplacian of divergence and θ_w thresholds were modified to 4.0×10^{-18} m^{-2} s^{-1} and 297 K, respectively. The masks also created discontinuities in the ITCZ location, with Berry and Reeder (2014) using a line joining program to connect lines that were within a given longitudinal and latitudinal distance from each other. A program similar to theirs is used for the current study.

Line joining is accomplished by iterating over all the remaining ITCZ identifications and determining if the eastern (western) most edge of one identification is within $\pm 3.5^\circ$ latitude and 3.5° longitude of the western (eastern) most edge of another (Berry and Reeder 2014). If two lines are joined in any given iteration, the following iteration is performed using the joined line as the reference for remaining lines. A diagram depicting the logic of the line joining program is shown in Figure 2.4 and an example follows.

Assume that there are five ITCZ identifications (lines A-E) remaining after ITCZ identification is performed. Line joining begins by iterating over lines A-E (iteration i in Figure 2.4), with a joined line tracker (x) initialized as an empty variable (i.e., no lines have been joined). On the first iteration, line A is checked to ensure that it has not been joined by checking if it is in the joined line tracker (x). If the line has not been joined, a joined line variable (y) is initialized to equal line A. If line A has been joined, iteration (i) continues to line B. In this case, (y) is set equal to line A because it is the very first iteration. The joined line variable (y) is then used as the reference for all line joining tests, with lines prepended and appended to (y) if they meet the joining criteria.

The next step is to perform a nested iteration over lines A-E to determine which lines should be joined (iteration j in Figure 2.4). In this case, line A is skipped as it

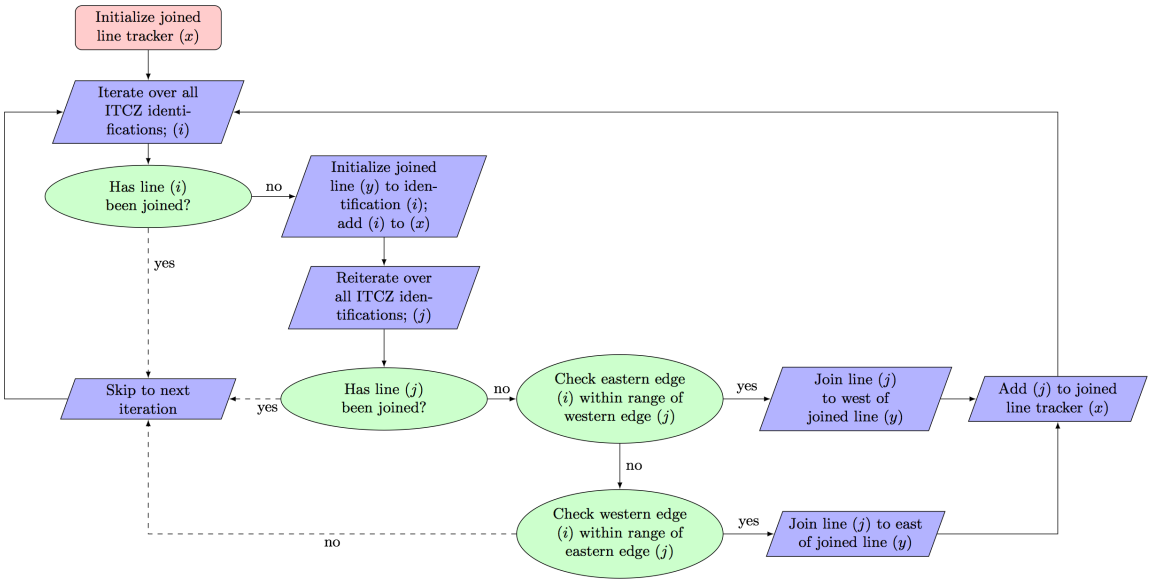

Figure 2.4: Outline of the line joining program used in the ITCZ identification method.

cannot be joined to itself. However, when line B is considered against the joined line variable (y), the two should be joined and therefore, line B is appended to (y). Line B is then added to the list of lines that have already been joined (x) so that it does not become joined to multiple different segments and the nested iteration continues and compares line C to (y). After the nested (j) iteration is completed, a check is performed to determined if line A (from iteration i) was joined to any other lines. If it was, line A is added to the list of lines that have been joined (x) and the joined line variable (y) is saved as an ITCZ identification. If line A was not joined, iteration (i) advances and line A is not added to the joined line tracker (x).

After the initial line joining, the program is run a second time, but on the newly joined lines. The same latitude threshold ($\pm 3.5°$) is used in the second joining, but a larger longitude threshold ($50°$) is chosen. This second pass of line joining is performed because visual inspection of the ITCZ identification method with only one

pass of line joining revealed many instances where TMI RRs indicated the ITCZ was present across the entire Pacific domain, but discontinuities were present over large expanses. Thus, the relaxed longitude threshold with the strict latitude threshold acts to remove the discontinuities without creating unrealistic identifications.

Figure 2.3d shows the final ITCZ location (black lines) and monthly mean TMI RRs (color); all identifications west of 160°E are not used as it is difficult to identify the ITCZ boundaries in the warm pool region based on RR data. There is good correspondence between the heaviest rainfall associated with ITCZ deep convection and the center location identified by application of this method to monthly mean reanalysis data. Visual inspection of all months in the TMI period showed that this method produced results similar to Figure 2.3 for nearly 90% of months with the remaining months showing some difficulty in identifying the ITCZ when it was weak or identifying the ITCZ center slightly north or south of the center of maximum TMI RRs.

This method of ITCZ identification is also able to identify both the northern and southern branches of double ITCZs and the SPCZ when more than one convergence zone is identified. Differentiation between ITCZ and SPCZ identifications is accomplished by comparing the orientation of the identifications to the typical location of the SPCZ. From Chen et al. (2008), the SPCZ is linearly positioned between 4°S; 140°E to 20°S; 160°W. Thus, if there is a high correlation and similar slopes between an identification in the region of 140°E-160°W and the idealized SPCZ location, the identification is marked as the SPCZ.

Although the ITCZ identification method is able to distinguish between branches of double ITCZs and the SPCZ, only the northern branch of the ITCZ is considered in this study, with the southern branch of the ITCZ and the SPCZ not included in this analysis. This is in contrast to Waliser and Gautier (1993) who did not

attempt to define a latitude for the ITCZ during double ITCZ periods. However, the identification used in this study is more objective, allowing separation of the northern and southern branches. Lastly, one month, March 1989, is excluded from the analysis as the northern branch of a double ITCZ was not identified due to the branch being very weak based on visual inspection of TMI RRs.

A test of the sensitivity of ITCZ identifications to the input reanalysis data was performed by applying the method to MERRA data and comparing the ITCZ

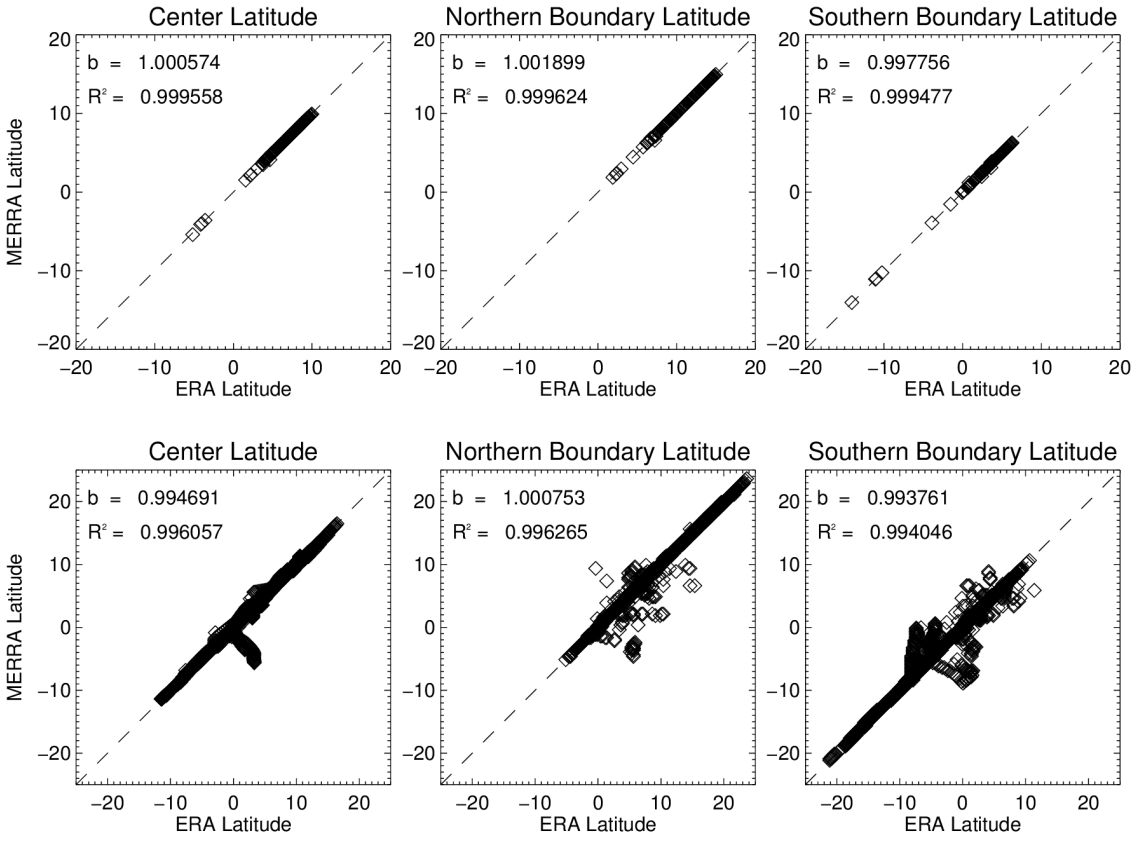

Figure 2.5: Comparison of ITCZ (left) center, (middle) northern boundary, and (right) southern boundary latitudes derived from (abscissa) ERA-Interim and (ordinate) MERRA variables. Comparisons are performed using (top) monthly zonal-mean values and (bottom) grid point values.

identifications to those produced by ERA-Interim data on both a monthly zonal-mean and point-to-point basis. These comparisons are shown in the left column of Figure 2.5. It is clear that monthly zonal-mean ITCZ identifications from the two reanalyses are nearly identical, with both the slope and coefficient of determination, R^2, values very near to one. The same is true when comparing the ITCZ identifications at the grid point level, however, there are some identifications that are clearly dissimilar between the datasets. These identifications were present in February 2001 and April 2012 and appear to be the result of errors in ITCZ identification in MERRA data based on comparisons between TMI RR imagery and ITCZ identifications.

2.5 Location of ITCZ Boundaries

Determination of ITCZ northern and southern boundaries is performed by first linearly interpolating the location of the ITCZ from the ERA-Interim data to the TMI or GPCP longitudinal grid spacing of 0.25° or 2.5°, respectively. This ITCZ center latitude is used as a starting point for iterations to the north and south to locate the ITCZ boundaries. The northern (southern) ITCZ boundary is located by finding the first grid box where the RR one grid box to the north (south) falls below a given threshold at every longitude where the ITCZ is present. Due to the spatial and temporal sampling of the TMI, even monthly mean RRs have some noise (Figure 2.3d color). Therefore, a smoother is applied to TMI RRs before ITCZ boundary identifications are performed to reduce local variations that can cause the boundary identification to fault. It is also important to ensure that ITCZ boundaries identified using different RR datasets are consistent to extend the climatology to different data sources and time periods. To do this, the sensitivity of ITCZ width to the RR dataset used for boundary identification and the smoothing width applied to the higher resolution TMI RRs was determined.

Figures 2.6a-c show monthly zonal-mean ITCZ widths from Dec. 1997 to Dec. 2012 computed from TMI (abscissa) and GPCP (ordinate) RRs using RR thresholds of 1, 2.5, and 5 mm day^{-1}, respectively. Colors correspond to the various smoothing widths applied to TMI RRs, with solid lines representing least-square regression fit. Table 2.2 shows the slopes and R^2 values for the regressions. From Figure 2.6a it appears that a RR threshold of 1 mm day^{-1} with a 9-point smoother applied to TMI RRs produces the most consistent widths between TMI and GPCP at this threshold,

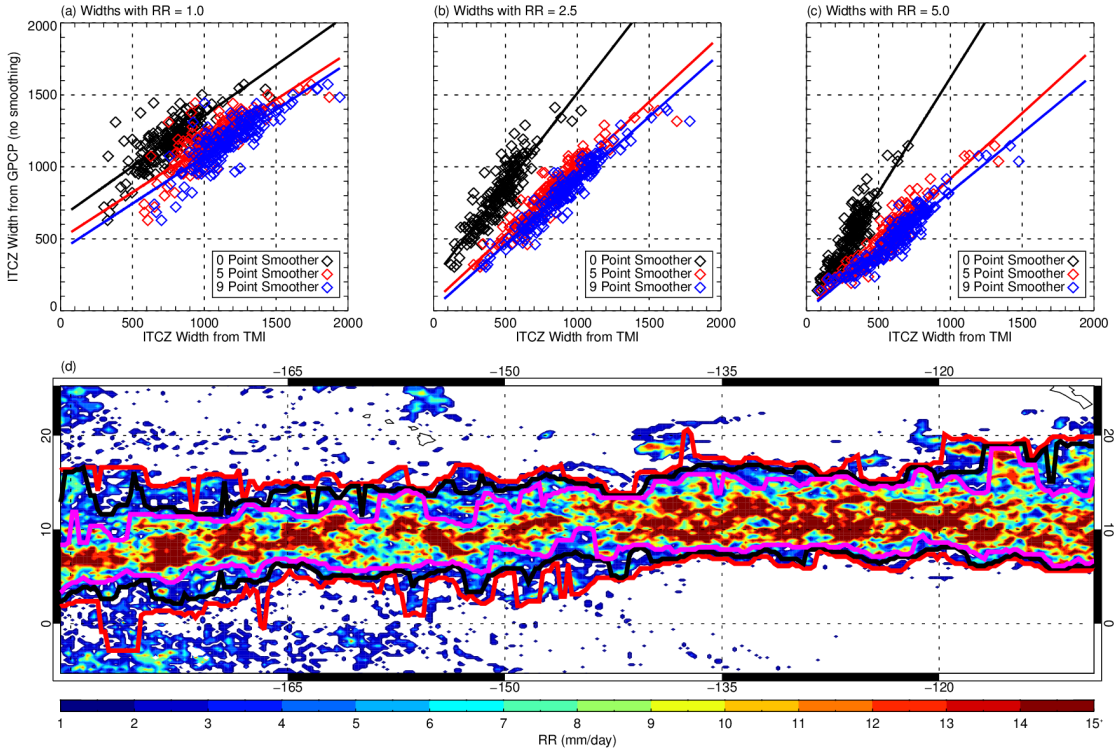

Figure 2.6: Relationships between monthly zonal mean ITCZ widths determined from GPCP and TMI RRs with a (a) 1 mm day^{-1} (b) 2.5 mm day^{-1} (c) 5 mm day^{-1} RR threshold. Solid lines in (a-c) are linear regressions with colors indicating the three different smoothing widths applied to TMI RRs. A contour map of TMI RRs (d) shows the location of the ITCZ boundaries for RR thresholds of 1 mm day^{-1} (red), 2.5 mm day^{-1} (black), and 5 mm day^{-1} (magenta) with a 5-point smoother applied to TMI RRs during the boundary identification.

Table 2.2: Slopes and R^2 values for linear regressions between monthly zonal-mean ITCZ widths identified from GPCP and TMI RRs using three different RR thresholds and three different smoothing widths on the TMI data (Figure 2.6).

Rain Rate (mm day^{-1})	1.0		2.5		5.0	
Smoothing Width	Slope	R^2	Slope	R^2	Slope	R^2
0	0.706	0.637	1.289	0.802	1.594	0.802
5	0.647	0.689	0.927	0.897	0.910	0.880
9	0.652	0.704	0.889	0.911	0.822	0.899

while TMI RRs with less or no smoothing produce more biased widths from those of GPCP. Although the slopes between TMI and GPCP derived widths are very similar (Table 2.2), the offsets when little to no smoothing is applied to TMI RRs must be reduced significantly for more consistent results between the datasets. With R^2 values from Table 2.2 less than or equal to 0.7, higher RR thresholds are studied in an attempt to maximize the R^2 value and obtain a slope near one. Figure 2.6b shows that a 2.5 mm day^{-1} RR threshold produces much more consistent results between the datasets. Widths derived using no TMI smoothing (black) are far below corresponding GPCP widths, which is most likely due to the resolution differences between the two data sets. Use of a 5-point smoother appears to produce a nearly 1-1 relationship between TMI and GPCP with a 9-point smoother producing TMI widths that are slightly larger than GPCP. From Table 2.2 it is clear that a 5-point smoother applied to TMI RRs maximizes both the slope (0.927) and R^2 values (0.897) compared to values at a 1 mm day^{-1} threshold.

To ensure that a 5-point smoother and RR threshold of 2.5 mm day^{-1} produce the most consistent results possible, Figure 2.6c is studied. Figure 2.6c is very similar to Figure 2.6b, with TMI widths derived using no smoothing or a 9-point smoother less than or greater than GPCP widths, respectively. Values from Table 2.2 confirm that

at a 5 mm day^{-1} RR threshold, the slope (0.910) and R^2 (0.880) values are maximized when a 5-points smoother is applied to TMI RRs, however, these values are lower than those using a 2.5 mm day^{-1} threshold. Therefore, a 5-point TMI smoothing width and 2.5 mm day^{-1} threshold are chosen for ITCZ boundary identifications. This is consistent with Zhou et al. (2011) who used a similar threshold of 2.4 mm day^{-1} to define the boundary of the ITCZ in GPCP RR data.

A comparison of the three RR thresholds tested for locating the ITCZ boundaries is shown in Figure 2.6d. Here, the 5-point smoother was applied to TMI RRs and boundaries were identified at 1 mm day^{-1} (red), 2.5 mm day^{-1} (black), and 5 mm day^{-1} (magenta). It is clear that the low threshold of 1 mm day^{-1} captures too much isolated precipitation north and south of the ITCZ, especially west of 165°E where the ITCZ and SPCZ converge. The opposite is true at a 5 mm day^{-1} threshold, which misses much of the precipitation along the edges of the ITCZ. Comparison between ITCZ widths calculated from both TMI and GPCP RRs (not shown) showed extremely similar values for the overlapping time period, with R^2 values of ≥ 0.75 for the northern and southern extents of the ITCZ as well as the full ITCZ width using the threshold of 2.5 mm day^{-1}.

When more than one ITCZ is identified, an ITCZ boundary check is run to ensure that the southern boundary of a given ITCZ is not located to the south of the northern boundary of other ITCZ identifications. Figure 2.7a shows the ITCZ identification for May 1998 when such a scenario occurs. Between 180°-120°W, there are three instances where the identified boundaries of the ITCZs cross. Thus, the overlapping boundaries are removed and these locations are recreated through linear interpolation between boundaries that do not overlap. This is shown in Figure 2.7b where all overlapping boundaries are removed. Although the interpolated boundaries are not as accurate as the initial identifications (i.e., the boundaries from $\sim 160°$ to

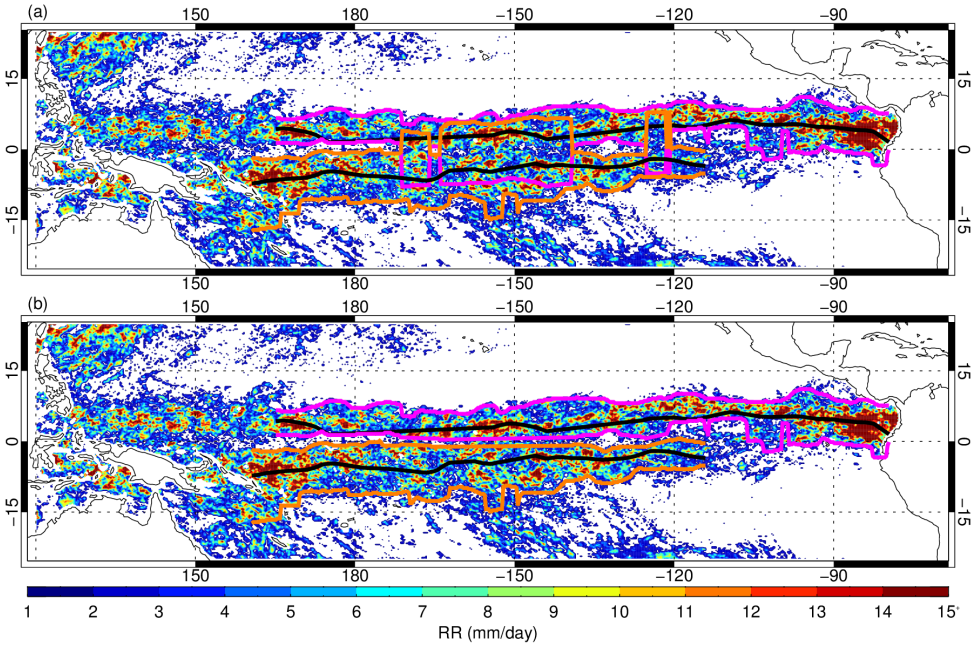

Figure 2.7: Example of ITCZ boundary overlapping problem for a double ITCZ on May 1998. Northern ITCZ boundaries are shown in magenta, with southern ITCZ boundaries shown in orange (a) before and (b) after overlapping boundary interpolation. ITCZ center location is in black.

$\sim$ 140°W are straight lines), they are much more accurate than the overlapping boundaries. This correction is applied in 1-5% of months for both the TMI and GPCP time periods.

Comparisons of ITCZ boundary identifications are shown in Figure 2.5 (Section 2.4) in the middle and right columns. The monthly zonal-mean (top) and grid point (bottom) comparisons of the ITCZ boundaries also produce slopes and R^2 values very near to one; however, there is much more scatter in the points than was observed in the center latitude comparison. The cause of the scatter was determined to be a result of the errors in the initial ITCZ identification; however, the errors in boundary identification depend on the magnitude of ITCZ identification errors and the extent of the ITCZ.

Figure 2.8 depicts three idealized ITCZ identification scenarios, with gray lines representing identifications from the reanalysis data and colors representing RR. ITCZ boundaries are located at the edges of the cool colors. In Figure 2.8a, the identification of the ITCZ is perfect, with boundaries identified at equal distances from the ITCZ center (gray arrows). Figure 2.8b illustrates the impact a small error in ITCZ identification has on the boundaries. Because the ITCZ identification is still located in an area where the RRs are greater than the threshold used to define the ITCZ boundaries, the boundaries are identified in exactly the same location as in Figure 2.8a; however, the distance to the boundaries are affected. Figure 2.8c represents a large error in ITCZ identification, which causes the ITCZ to be located outside of the actual ITCZ RR band. In this case, all RRs to the north and south of the ITCZ are below the RR threshold and results in ITCZ boundaries very near to the inaccurate ITCZ identification. As previously mentioned, only two months (February 2001 and April 2012) suffered from this type of error in MERRA derived ITCZ identifications, with no errors of this type in ERA-Interim derived identifications.

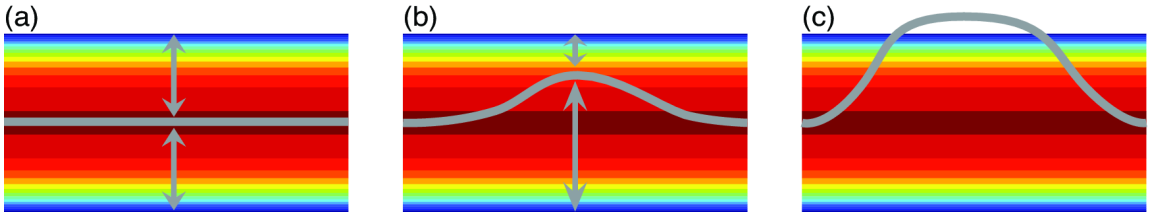

Figure 2.8: Idealized example of error in ITCZ identification and its impacts on boundary identifications. Warm (cool) colors indicate large (small) RRs; the end of the color gradient represents the ITCZ boundary. The solid gray lines indicate ITCZ identifications with gray arrows representing the distance to the ITCZ boundary. The three panels depict (a) perfect ITCZ identification, (b) an error in ITCZ identification, but correctly identified boundaries, and (c) a large error in the ITCZ identification with errors in boundary identification.

2.6 ITCZ Precipitation Intensity

The intensity of ITCZ convection will primarily be studied using RRs, rather than a more direct measure like radar PF characteristics, to extend the analysis to the 36-year GPCP period. Although there are more direct measures of convective intensity than RR (i.e., maximum storm height and maximum height of the 30-dBZ echo), such metrics would limit this study to the 15-years of TRMM data available. There have also been many studies linking the aforementioned metrics to RR, which makes it a reasonable proxy. The maximum height of storms has been used in satellite RR algorithms for many years (e.g., Griffith et al. 1978; Adler and Mack 1984) and has been directly related to observed RRs using radar observations (Cheng and Houze Jr. 1979; Leary 1984; DeMott and Rutledge 1998). DeMott and Rutledge (1998) also found a strong correlation between the height of the 30-dBZ echo and rainfall rate with higher RRs correlated with higher 30-dBZ echo heights. Updraft velocity was also linked to RR by Short et al. (1997), indicating that stronger updrafts leads to heavier rainfall. Based on these results, RR should provide a reliable measure of the intensity of the ITCZ convection.

Recent modeling studies have noted an intensification of precipitation near the center of the ITCZ with precipitation near the edges of the ITCZ decreasing (Neggers et al. 2007; Lau et al. 2013; Lau and Kim 2015). This phenomena has been referred to as the "rich-get-richer" mechanism. Thus, in an attempt to assess the convective intensity near the center of the ITCZ, the ITCZ is separated into two regions: the central ITCZ within $\pm 1^{\circ}$ latitude of the ITCZ center and the full ITCZ between the northern and southern boundaries. Within these areas, monthly means of all gridboxes are computed to determine the monthly mean ITCZ RR.

3. RESULTS

The climatological mean center location, width, and precipitation intensity of the ITCZ are calculated over the entire longitudinal extent of the ITCZ to obtain general ITCZ characteristics, while long-term and seasonal ITCZ characteristics are calculated over both the entire longitudinal extent and central and eastern Pacific (hereafter CPAC and EPAC) domains for easier comparison to previous studies (e.g., Waliser and Gautier 1993; Zhou et al. 2011). A depiction of the CPAC and EPAC domains used is shown in Figure 3.1. The warm pool region of the Pacific is excluded as it can be difficult to define the ITCZ through both visual and automated analysis.

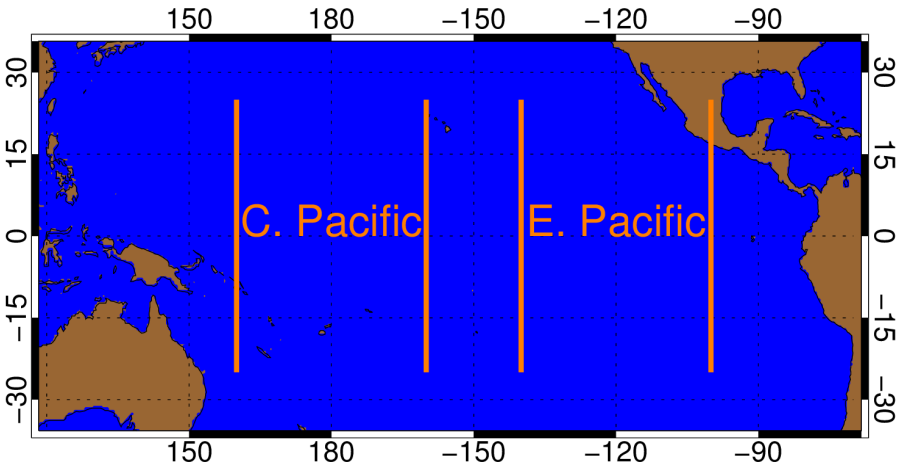

Figure 3.1: Boundaries of the central and eastern Pacific domains used.

From Table 3.1 there is evidence of a narrowing in the ITCZ based on the differences in ITCZ width between the GPCP and TMI periods. This is a result of the locations of the northern and southern ITCZ boundaries contracting toward the center of the ITCZ as indicated by the larger widths in the full 36-year period com-

Table 3.1: Climatology of ITCZ characteristics for GPCP and TMI derived values ($\pm\sigma$).

		Central/Full	Northern	Southern
GPCP	Latitude (°)	6.63 ± 2.97	11.17 ± 3.95	3.41 ± 3.83
	Width (km)	871.46 ± 393.85	509.15 ± 259.56	362.26 ± 233.78
GPCP (TMI Period)	Latitude (°)	6.66 ± 2.75	10.93 ± 3.83	3.68 ± 3.70
	Width (km)	815.49 ± 393.43	479.65 ± 256.81	335.85 ± 224.57
TMI	Latitude (°)	6.72 ± 2.84	10.60 ± 3.60	3.25 ± 3.46
	Width (km)	818.71 ± 361.14	431.56 ± 236.38	387.17 ± 193.21

pared to the smaller widths during the TMI period, which only includes the last 15 years of the GPCP period. The mean values for the central latitude of the ITCZ do not indicate any large shifts between the time periods. The northern and southern widths, or extents, of the ITCZ, defined as the distance from the center of the ITCZ to the northern and southern boundaries, also show evidence of contraction between the GPCP and TMI time periods; however, this only appears in the GPCP derived values; i.e., GPCP derived values over the entire GPCP period versus GPCP derived values over the TMI period. In the TMI derived extents, the northern extent contracts, relative to the full GPCP period, while the southern extent expands. The cause of these differences is unclear, but may be due to possible RR biases that are discussed later. Only ITCZ characteristics derived from GPCP RRs are used for the long-term and seasonal analyses of this study as the GPCP time series is more than twice the length of TMI (181 TMI months versus 431 GPCP months). Due to monthly changes in the longitudinal extent of the ITCZ (Wang and Magnusdottir 2006), the ITCZ may not be present in or cover the entire longitudinal extent of the CPAC and EPAC domains every month. Therefore, months where the ITCZ is not identified in a given domain are excluded from the long-term and seasonal analyses.

3.1 Latitude, Width, and RR Climatology

Frequency distributions of monthly zonal mean ITCZ center, northern, and southern latitudes, extents, and RRs are presented in Figure 3.2. Because of the differences in length of the TMI and GPCP datasets, normalized distributions are plotted for GPCP data over both the full GPCP (bold) and TMI (light) periods for a more direct comparison between GPCP and TMI (dotted) derived characteristics. Both

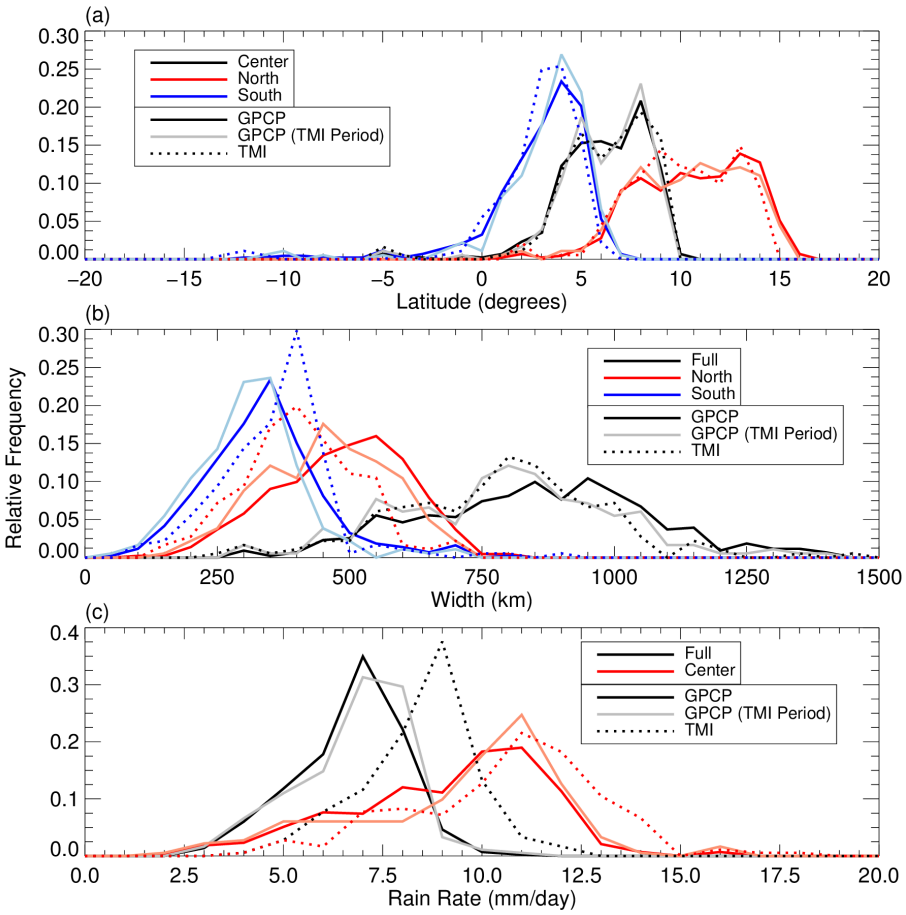

Figure 3.2: PDFs of monthly mean ITCZ (a) latitude, (b) width, and (c) rain rate determined using GPCP data over the full GPCP period (bold solid), GPCP data over the TMI period (light solid), and TMI data over the full TMI period (dashed) with colors corresponding to different locations.

the TMI and GPCP derived northern and southern ITCZ latitudes (Figure 3.2a) are in fairly good agreement even when comparing the full GPCP period to the TMI data. Right tails of GPCP derived latitude distributions for both the northern and southern ITCZ boundaries are skewed slightly toward northern values compared to TMI for both periods. Central latitudes also agree well between TMI and GPCP; however, central ITCZ latitude identifications are independent of RRs as they are derived from the ERA-Interim.

Full ITCZ widths from TMI and GPCP over the TMI period have nearly identical distributions (light and dotted lines Figure 3.2b) with widths from the full GPCP period peaking at slightly larger widths (bold Figure 3.2b). The main differences between the two periods occur at widths over 900-km, suggesting these greater widths were more common prior to the TMI period. The width of the northern (southern) extent of the ITCZ from TMI also shows a slight shift toward smaller (larger) widths relative to GPCP; a smaller difference is observed when comparing GPCP data from the same period. These shifts give the TMI-derived widths slightly more symmetry; however, this may be an artifact of RR biases between the datasets as zonal mean GPCP and TMI RRs (Figure 3.3a) indicate slightly larger GPCP RRs near ITCZ boundaries. Also, ITCZ width and latitude characteristics derived from TMI RRs re-gridded to the same resolution as GPCP (Figure 3.3b) produced results similar to the smoothed TMI RR data described above, indicating that the TMI RR retrievals may be biased low relative to GPCP for lightly raining systems found on the edges of the ITCZ. It is important to note that the differences between GPCP and TMI derived widths magnify these differences since a difference of 1-2° translates to a much larger difference in absolute distance.

Figure 3.2c shows the frequency distributions of monthly mean RRs within the ITCZ boundaries in the black lines and within ±1° from the center of the ITCZ

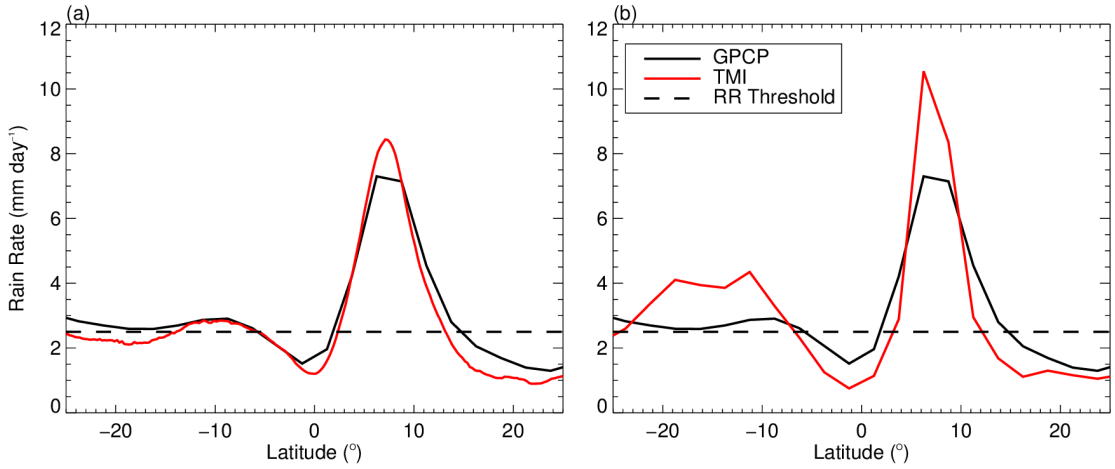

Figure 3.3: Climatological mean of zonal mean RRs from GPCP (black) and TMI (red) averaged over 160°E-80°W and the TMI period. GPGP RRs are used at their native resolutions while TMI RRs are (a) at their native resolutions and (b) re-gridded to GPCP resolution. Dashed line represents the 2.5 mm day^{-1} RR threshold used to identify ITCZ boundaries.

(hereafter referred to as the central ITCZ RR) in the red lines from GPCP and TMI. The mean RRs near the center of the ITCZ are roughly twice the mean RRs over the entire ITCZ, indicating more intense precipitation. Comparing the RRs at the center of the ITCZ, the GPCP period and TMI periods have roughly the same distribution; however, RRs greater than 11 mm day^{-1} occur more frequently in the TMI data than in GPCP over both periods, which is likely related to the RR biases discussed above. RRs over the entire ITCZ differ considerably with the most frequent TMI RR roughly 2 mm day^{-1} larger than the most frequent GPCP RR (9 mm day^{-1} versus 7 mm day^{-1}). These differences in RR distributions imply an over estimation of RRs in the TMI data or an under estimation of RRs by the GPCP product, with Hilburn and Wentz (2008) supporting the former, but to a lesser extent than seen here. Values derived from TMI RRs re-gridded to GPCP resolution produced similar distributions, which also indicates RR biases between the TMI and GPCP datasets.

However, these biases do not affect the overall trends and interpretation of the results as shown in the similarities between GPCP and TMI derived time series later in this section.

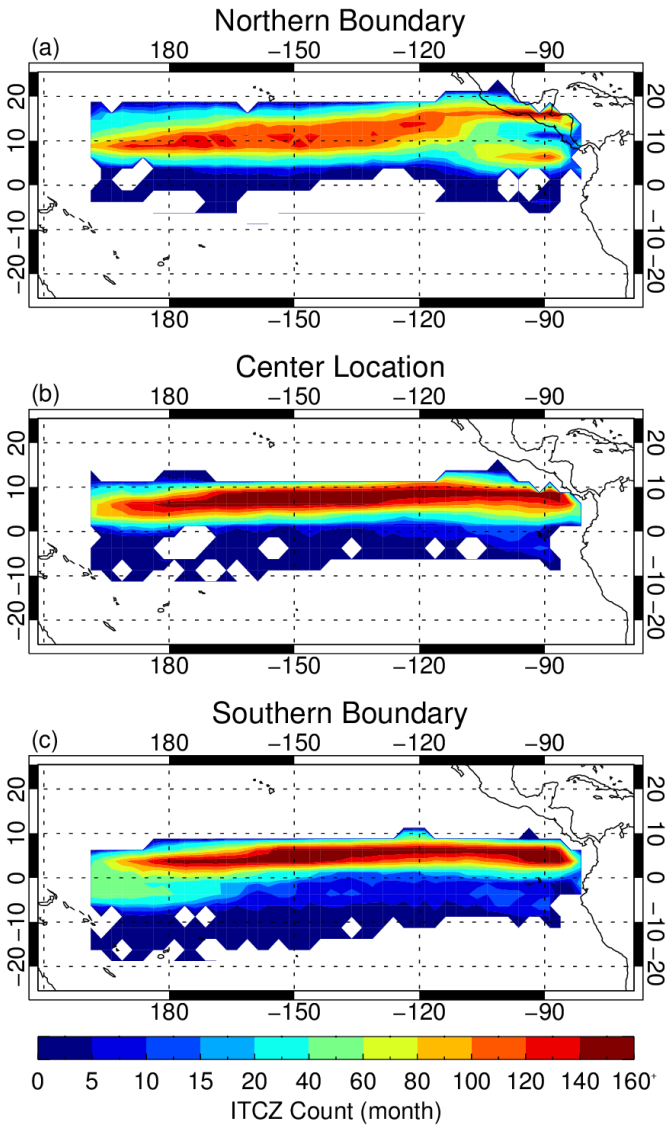

Figure 3.4: Count of ITCZ identification from GPCP for the (a) northern boundary, (b) center, and (c) southern boundary.

Figure 3.4 shows the number of months that the ITCZ center and boundaries are located in a given $2.5^\circ \times 2.5^\circ$ grid box, putting Figure 3.2a in a spatial context. For example, Figure 3.4a shows that the majority of northern boundary identifications located north of 15°N are east of 120°W, with Figure 3.4c showing that the majority of southern boundary identifications located south of the equator are west of 165°W. The bifurcation of ITCZ northern boundary identifications near the Americas is due to seasonal variability, with identifications in JJA and SON located predominantly north of 10°N and identifications in DJF and MAM located predominantly south of 10°N.

3.2 Long-term Trends in ITCZ Characteristics

Time series of monthly zonal mean ITCZ center latitude, width, and ITCZ RR over the entire longitudinal extent of the ITCZ are shown in Figure 3.5. As expected, the location of the ITCZ (Figure 3.5a) from GPCP (black) and TMI (red) are nearly identical since the center location of the ITCZ depends only on ERA-Interim derived variables. ITCZ widths in Figure 3.5b are also extremely similar between the GPCP and TMI derived characteristics. However, this is not the case for the northern (Figure 3.5c) and southern (Figure 3.5d) extents, with the differences in ITCZ boundary identifications between the RR datasets causing differences in the extents. Because the time series indicate a translation between the datasets with only minor changes in the shape of the curves, these differences will have little impact on trends derived from the two datasets. An interesting feature of the full ITCZ width (Figure 3.5b) is that there appears to be less interannual variability in the width of the ITCZ after the large El Niño event in 1997/1998. This shift can also be seen in the northern (Figure 3.5c) and southern (Figure 3.5d) extents.

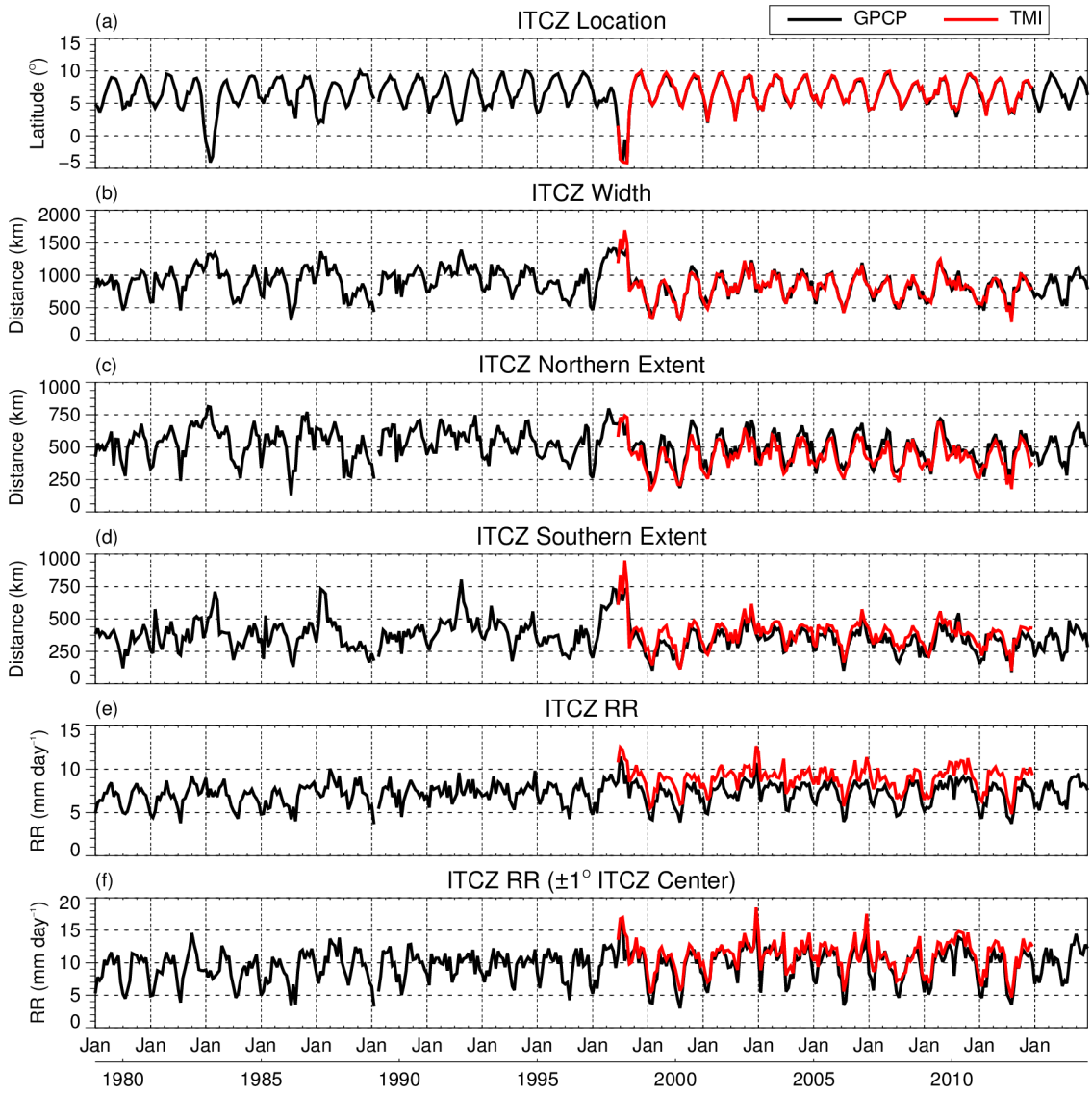

Figure 3.5: Time series of monthly mean (a) central ITCZ latitude, (b) full ITCZ width, (c) extent of the northern half of the ITCZ, (d) extent of the southern half of the ITCZ, (e) RR over the entire ITCZ, and (f) central ITCZ RR for GPCP data (black) and 5-point smoothed TMI data (red) using a RR threshold of 2.5 mm day^{-1}.

Figures 3.5e-f show RRs over the full and central ITCZ, respectively. The differences in ITCZ RR distributions in Figure 3.2c appear clearly in Figure 3.5e, with TMI RRs slightly greater than GPCP RRs for almost every month; however, the

time series are extremely similar. Figure 3.5f is consistent with Figure 3.2c, with GPCP and TMI derived center ITCZ RRs having nearly identical monthly values.

Time series analyses of ITCZ characteristics in the CPAC and EPAC are shown in Figures 3.6 and 3.7, respectively. One major difference between the domains is the number of months in the CPAC where the ITCZ was not identified (i.e., missing

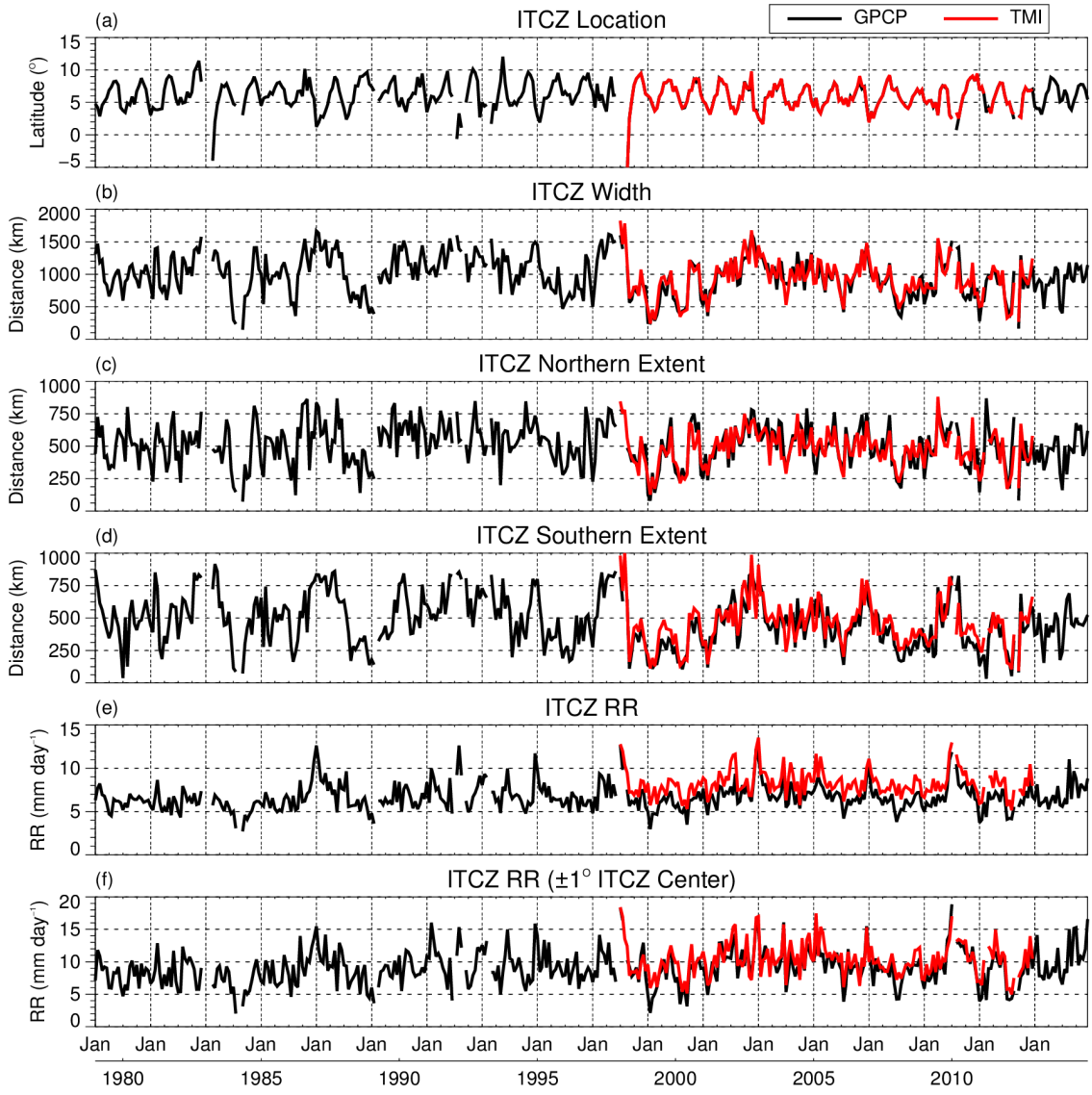

Figure 3.6: As in Figure 3.5 but for the CPAC domain.

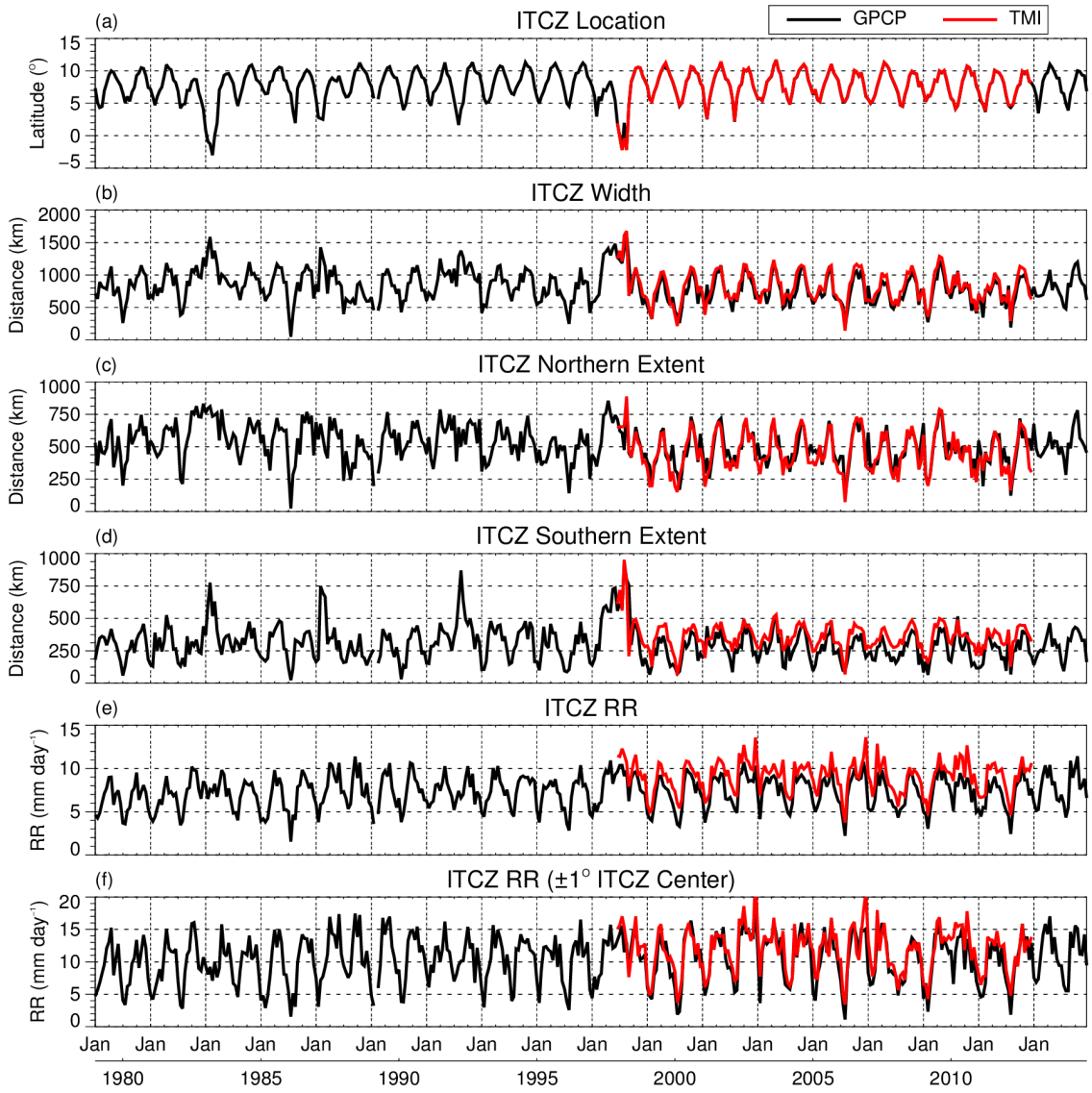

Figure 3.7: As in Figure 3.5 but for the EPAC domain.

data points in the time series) is much greater than the EPAC; 13-1 for the GPCP period and 4-0 for the TMI period. This is due to the varying longitude extent of the ITCZ mentioned above. As in Figure 3.5a, the locations of the ITCZ in the CPAC (Figure 3.6a) and EPAC (Figure 3.7a) are identical between the GPCP and TMI data due to the ERA-Interim dependence. It does, however, appear that the

ITCZ is located slightly farther to the south in the CPAC than in the EPAC. In the CPAC, the width of the ITCZ (Figure 3.6b) is highly variable, with no discernible seasonal cycle, whereas in the EPAC (Figure 3.7b) there is less variability, with a clear seasonal cycle. Similar comparisons can be made for the northern and southern extents of the ITCZ (panels c-d). As was noted for the full Pacific ITCZ, a shift in the variability of ITCZ width after 1998 is present in the CPAC and EPAC, although the shift in the EPAC is more pronounced than in the CPAC. When comparing ITCZ RRs in the CPAC and EPAC, both the full (panel e) and central (panel f) ITCZ RRs appear to have a larger range in the EPAC (Figure 3.7) than in the CPAC (Figure 3.6). However, as in the width time series, there is a very weak seasonal cycle in CPAC ITCZ RRs while one is clearly present in the EPAC. The variability shift observed in widths does not appear in ITCZ RRs for either domain.

For the remainder of this study, all long-term time series are converted to anomalies by removing their mean annual cycle. Trends are then determined based on these anomalies with the statistical significance of the trends determined using a students t-test (Zhou et al. 2011). To determine the degrees of freedom for the t-test, the number of samples in the time series is divided by two times the lag at which the auto correlation falls to e^{-1}. This acts to reduce the degrees of freedom to compensate for auto correlated samples, which are not independent (Leith 1973).

3.2.1 ITCZ Latitudes

Figure 3.8 shows the monthly anomalies for the center, northern boundary, and southern boundary latitudes averaged over the entire longitudinal extent of the ITCZ in black with their trends in red. Slopes and p-values for the trend lines are in Table 3.2. Examination of the ITCZ center latitude (Figure 3.8a) shows an extremely weak trend that is not significant even at the 90% confidence level. Figures 3.8b-c show

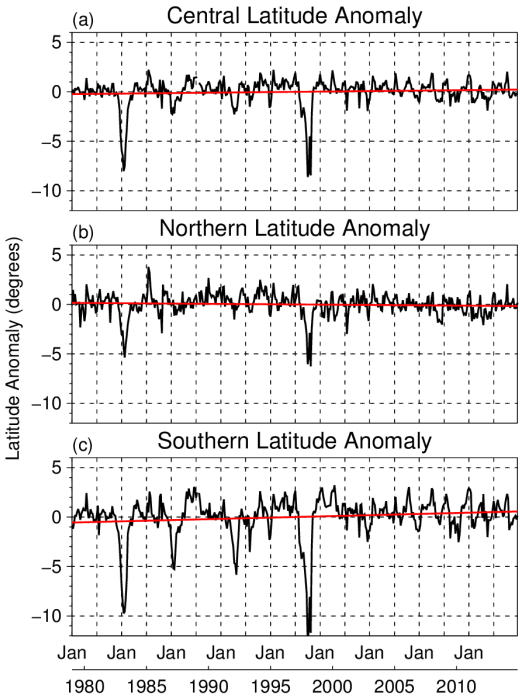

Figure 3.8: Monthly latitude anomalies (black) over the full longitudinal extent of the ITCZ for the (a) center, (b) northern boundary, and (c) southern boundary of the ITCZ. Least squares regressions are also shown (red), with trends and significance values are shown in Table 3.2.

Table 3.2: Slopes and p-values for monthly mean latitude anomalies from Figure 3.8. Slopes are in units of degrees decade^{-1}.

	Center Latitude	Northern Boundary	Southern Boundary
Slope (b)	0.126	-0.089	0.313
p-value	0.739	0.283	0.381

the latitude anomalies for the northern and southern boundaries, respectively. For the northern boundary of the ITCZ there is essentially no trend; however, there appears to be a clear positive trend in the southern boundary of the ITCZ, but neither of the trends are significant (90% confidence level). The total migration of

the center, northern and southern boundaries of the ITCZ over the 36 year period are 0.5°, 0.3°, and 1.1°, respectively. For all three latitude characteristics there is a clear ENSO signal, namely for the strong El Niños in 1982/1983 and 1997/1998. What is most interesting about these plots is that the influence of ENSO appears to have only a small impact on the northern ITCZ boundary (Figure 3.2b), with the impact increasing in the center latitude (Figure 3.2a) and appearing most prominently in the southern boundary (Figure 3.2c). This increased influence when approaching the equator is clear when noting that the northern boundary and center of the ITCZ seem to have been effected by only the 1982/1983 and 1997/1998 El Niños, while signs of the 1987 and 1991 events are present in the southern boundary. This is likely due to ENSO events being characterized by equatorial SST anomalies (Bjerknes 1969) and the influence that SSTs have on both lower-tropospheric convergence and convection (Graham and Barnett 1987; Back and Bretherton 2009). These changes, coupled with the climatological location of the ITCZ ($\sim 8°$N), place the ITCZ southern boundary closest to El Niño related changes, with the ITCZ center and northern boundary at second and third closest, respectively. As discussed in Section 3.3, removal of the ENSO signal does not change the signs of trends, only the magnitudes and significance values.

ITCZ latitude anomalies are further separated into the CPAC and EPAC domains in Figure 3.9 with trends in Table 3.3. In the CPAC the location of the ITCZ (Figure 3.9a) has not changed very rapidly, moving roughly 0.35° south in the past 36 years. However, the northern and southern ITCZ boundaries (Figures 3.9b-c) have migrated toward the center of the ITCZ by roughly 0.8° and 1.2°, respectively. The center location of the ITCZ in the EPAC (Figure 3.9d) has migrated about 0.5° north, with the northern and southern boundaries (Figures 3.9e-f) also migrating toward the center of the ITCZ by 0.5° and 1.0°, respectively. It is worth noting that none of the

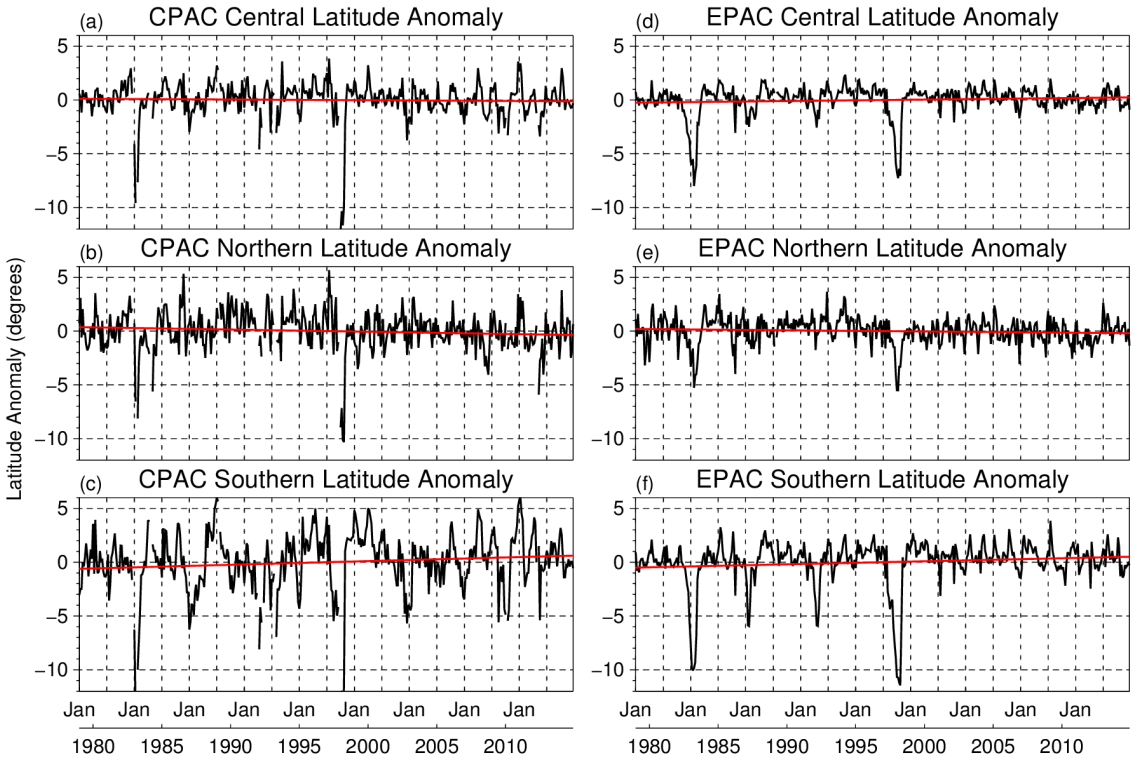

Figure 3.9: Monthly latitude anomalies for the (top) full, (middle) northern, and (bottom) southern widths of the ITCZ in the (a-c) central and (d-f) eastern Pacific. Black lines are anomalies while red lines are trends. Trends and significance values are shown in Table 3.3.

Table 3.3: Slopes and p-values for monthly mean latitude anomalies from Figure 3.9. Slopes are in units of degrees decade^{-1}.

		Center Latitude	Northern Boundary	Southern Boundary
CPAC	Slope (b)	-0.097	-0.230	0.320
	p-value	0.742	0.250	0.373
EPAC	Slope (b)	0.135	-0.118	0.284
	p-value	0.518	0.457	0.386

trends in ITCZ latitude in both the CPAC and EPAC are significant (90% confidence level). The influence of ENSO is also clearly seen in both the CPAC and EPAC in

Figure 3.9, with the CPAC exhibiting a larger amount of interannual variability than the EPAC.

3.2.2 ITCZ Extents

Monthly anomalies of ITCZ width over the entire longitudinal extent of the ITCZ are shown in Figure 3.10, with trends and p-values values in Table 3.4. The full extent of the ITCZ is defined as the distance between the northern and southern boundaries while the northern and southern extents of the ITCZ are defined as the distance from the center of the ITCZ to the northern and southern boundaries, respectively. Because of these definitions, the northern and southern extents are dependent on

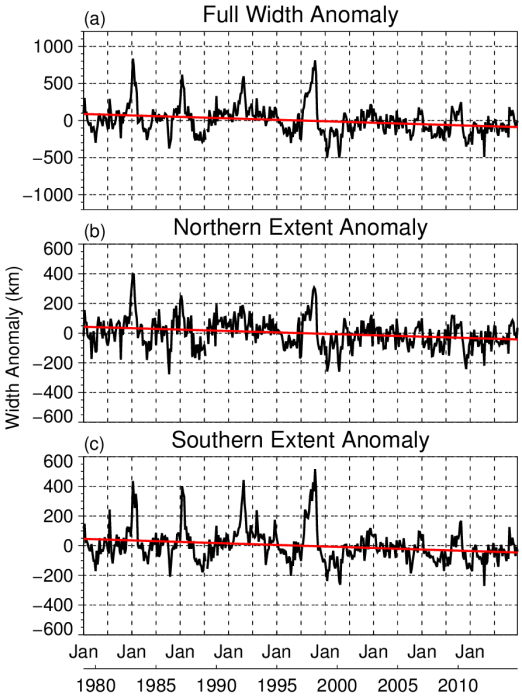

Figure 3.10: Monthly width anomalies (black) over the full longitudinal extent of the ITCZ for the (a) full, (b) northern, and (c) southern widths of the ITCZ. Least squares regressions are also shown (red), with trends and significance values are shown in Table 3.4.

Table 3.4: Slopes and p-values for monthly mean width anomalies from Figure 3.10. Slopes are in units of km decade^{-1}.

	Full Width	Northern Extent	Southern Extent
Slope (b)	-43.909	-23.902	-20.007
p-value	0.124	0.036	0.171

both the location of ITCZ boundaries and the location of the ITCZ center, while the full width depends only on the location of the boundaries.

From Figure 3.10a, the width of the ITCZ decreased by 158 km over the past 36 years. This narrowing was expected based on the negative (positive) trends in the location of the northern (southern) ITCZ boundary (Figure 3.8). The reason for the significant trend in ITCZ width, while the trends in ITCZ boundaries were not is due to the aforementioned difference between degrees and absolute distance, with a small change in degrees translating to a large change in absolute distance. The narrowing of the northern extent of the ITCZ (86 km, Figure 3.8b) is similar to that of the southern extent (72 km, Figure 3.8c). This means that, on average, the northern and southern extents under went roughly symmetric contraction.

ENSO signals are also present in the ITCZ extents, which was expected based on their presence in ITCZ latitudes. ENSO influences on width are similar to those in latitude, with the southern extent most influenced and the northern extent least influenced. However, the total width of the ITCZ is also influenced by ENSO due to the width dependence on the location of the southern boundary.

Separation of the ITCZ widths into the CPAC and EPAC domains (Figure 3.11, trends in Table 3.5) reveals that the CPAC width of the ITCZ has decreased by 215 km (Figure 3.11a), with the reduction in the northern extent (50 km, Figure 3.11b) much smaller than that of the southern extent (160 km, Figure 3.11c). The

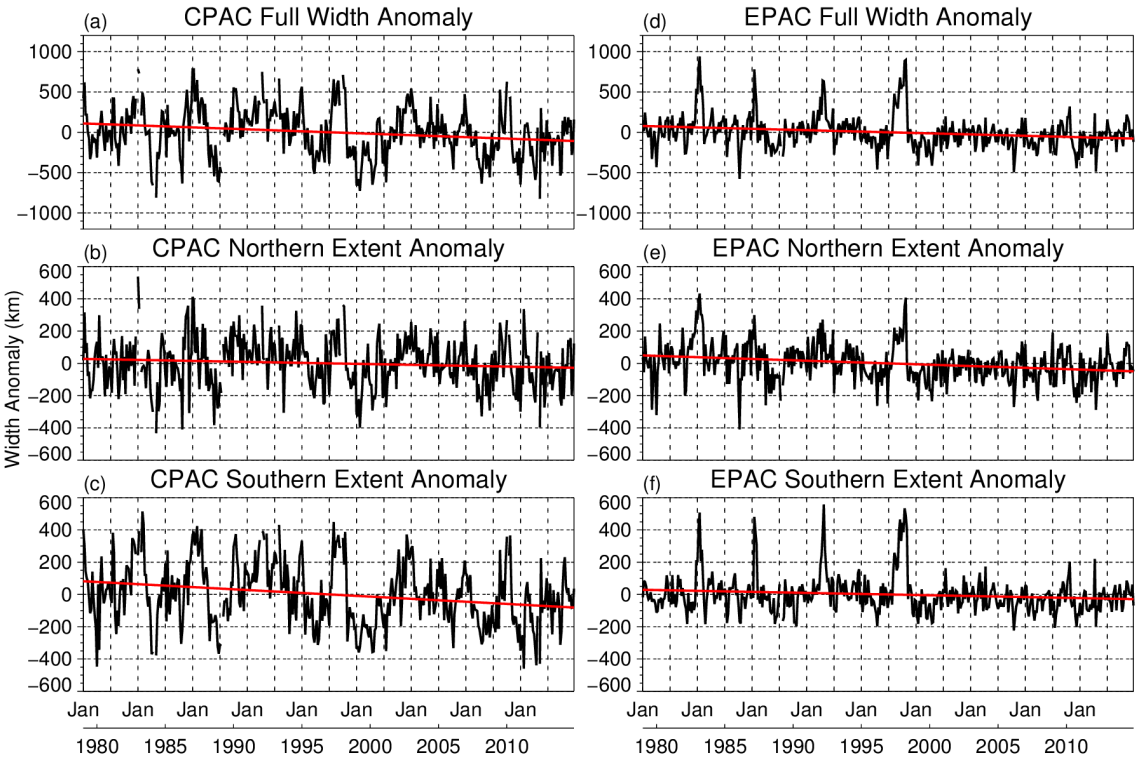

Figure 3.11: Monthly width anomalies for the (top) full, (middle) northern, and (bottom) southern widths of the ITCZ in the (a-c) central and (d-f) eastern Pacific. Trends and significance values are shown in Table 3.5.

Table 3.5: Slopes and p-values for monthly mean width anomalies from Figure 3.11. Slopes are in units of km decade^{-1}.

		Full Width	Northern Extent	Southern Extent
CPAC	Slope (b)	-59.786	-14.760	-45.026
	p-value	0.185	0.288	0.120
EPAC	Slope (b)	-44.659	-28.500	-16.158
	p-value	0.064	0.037	0.234

differences in the contraction of the northern and southern extents are a result of the central location of the ITCZ migrating in the same direction as the northern boundary (Figures 3.9a-b). A similar combination of changes occurs in the EPAC,

but with a greater expansion of the ITCZ's northern extent.

As in the CPAC, the migration of the ITCZ boundaries causes a 160 km reduction (90% confidence level) in the width of the ITCZ in the EPAC (Figure 3.11d). However, the northern migration of the ITCZ in the EPAC (Figure 3.9d) causes a more rapid contraction in the northern extent (100 km significant at 90% confidence level, Figure 3.11e) than in the southern extent (58 km, Figure 3.11f). Because the boundaries of the ITCZ have migrated in the same direction in the CPAC and EPAC, the differences between the trends in the northern and southern extents between the two regions are the result of the opposite trends in the central location of the ITCZ. It is worth noting that width anomalies in both the CPAC and EPAC appear to be smaller in the latter period of the time series (after about 1998), with a more prominent reduction in anomalies in the EPAC. Signs of ENSO appear again in the CPAC and EPAC widths, however, the signal is much clearer in the EPAC due to the greater interannual variability present in the CPAC.

3.2.3 ITCZ Rain Rates

Monthly RR anomalies over the entire longitudinal extent of the ITCZ, separated into RRs over the central and full ITCZ, are shown in Figure 3.12, with trends and p-values in Table 3.6. The mean RR over the central region of the ITCZ, where the most intense convection should be located, has increased more rapidly than the mean

Table 3.6: Slopes and p-values for monthly mean RR anomalies from Figure 3.12. Slopes are in units of mm day^{-1} decade^{-1}.

	Full RR	Central RR
Slope (b)	0.147	0.310
p-value	0.191	0.120

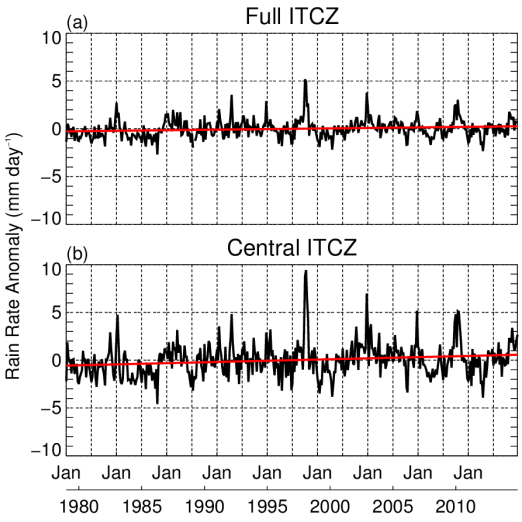

Figure 3.12: Monthly RR anomalies (black) over the full longitudinal extent of the ITCZ for the (a) full and (b) central ITCZ. Least squares regressions are also shown (red), with trends and significance values in Table 3.6.

RR over then entire ITCZ, with increases of 1.1 mm day^{-1} and 0.5 mm day^{-1} in the past 36 years, respectively. While both of these trends are not significant at the 90% confidence level, the trend over the center of the ITCZ is slightly more robust (p=0.120) than over the entire ITCZ (p=0.191).

After separating ITCZ RRs into the CPAC and EPAC domains (Figure 3.13), examination of GPCP RR anomalies in the CPAC shows that the long-term trends in RRs over the full ITCZ (Figure 3.13a) and central ITCZ (Figure 3.13b) have increased roughly 0.5 mm day^{-1} and 1.6 mm day^{-1}, respectively. However, neither of these trends are significant at the 90% confidence level. (Table 3.7). In the EPAC, trends in RR over the full (Figure 3.13c) and central (Figure 3.13d) ITCZ are similar to trends in the CPAC, with RRs in the center of the ITCZ increasing more rapidly than over the full ITCZ, but both trends in the EPAC are significant (90% confidence level). There does not appear to be any change in the variability of RR anomalies

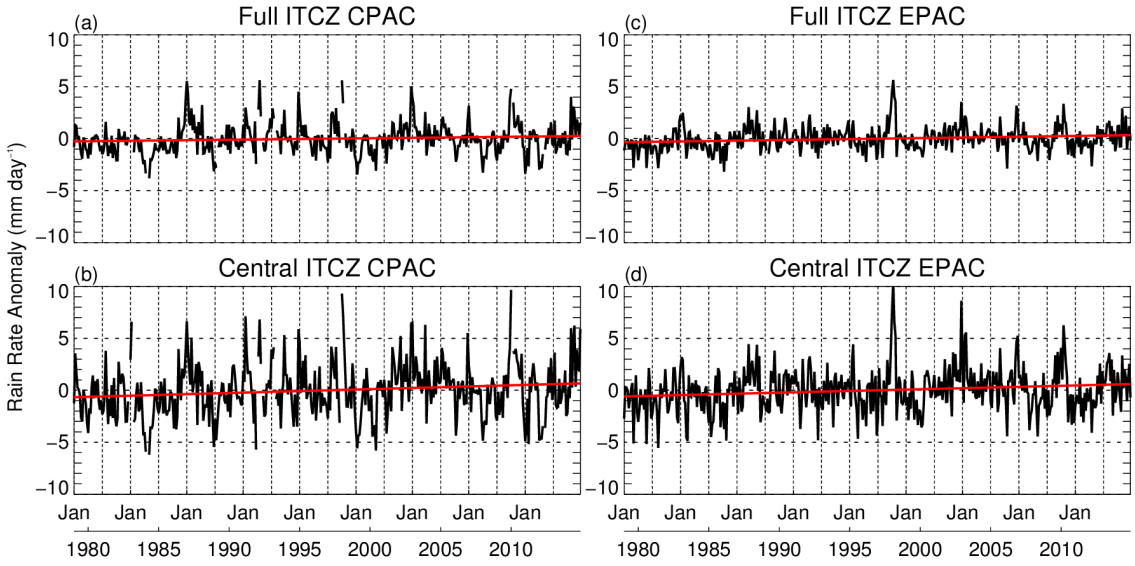

Figure 3.13: Monthly RR anomalies for the (top) full and (bottom) central ITCZ in the (a-b) central and (c-d) eastern Pacific. Trends and significance values are shown in Table 3.7.

Table 3.7: Slopes and p-values for monthly mean RR anomalies from Figure 3.13. Slopes are in units of mm day^{-1} decade^{-1}.

	CPAC		EPAC	
	Full ITCZ	Central ITCZ	Full ITCZ	Central ITCZ
Slope (b)	0.143	0.440	0.188	0.340
p-value	0.408	0.127	0.079	0.018

after 1997/1998 as was shown in width anomalies discussed above.

3.3 Influence of ENSO

Previous studies (e.g., Zhou et al. (2011) and Bain et al. (2011)) handle the influence of ENSO on ITCZ trends differently, so the sensitivity of results to ENSO's influence is tested. First, monthly anomalies of ITCZ latitudes and extents are correlated with the Multivariate ENSO Index(MEI; Wolter and Timlin (1993, 1998))

to determine if these ITCZ characteristics are influenced by ENSO; regression to the Niño 3.4 index was also performed with similar results. Figure 3.14 shows MEI time series (color) with ITCZ latitude anomalies (black line) in the left column and ITCZ width anomalies (black line) in the right column. It is clear that ENSO does influence the location of the ITCZ's southern boundary, with positive MEI values (i.e., El Niño conditions) corresponding to negative latitude anomalies. There is also evidence that ENSO has some influence on the center latitude, but there is little evidence of an influence on the northern boundary (Figures 3.14a-c). For ITCZ widths, there is a moderate ENSO influence on the full ITCZ width, and the

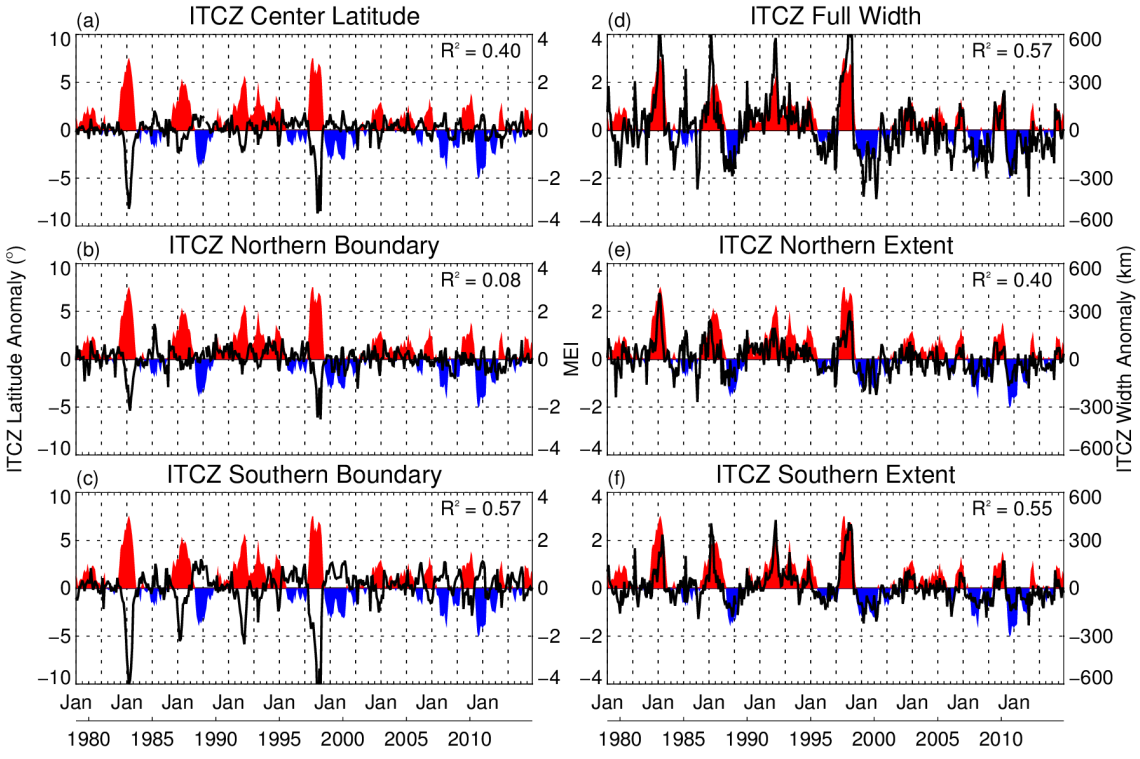

Figure 3.14: MEI (color) and ITCZ anomalies (black) for (a) center latitude, (b) northern boundary latitude, (c) southern boundary latitude, (d) full width, (e) northern extent, and (f) southern extent. R^2 values are shown in the upper right corner of each plot.

northern and southern extents (Figures 3.14d-f), with positive MEI corresponding with positive width anomalies. Time series of ITCZ RR anomalies and the MEI are shown in Figure 3.15 and interestingly indicate that ENSO has a much weaker influence on ITCZ RR compared to the other characteristics. With evidence of an ENSO influence on ITCZ latitudes and widths, the ENSO signal is removed to test its influence on trends in ITCZ characteristics.

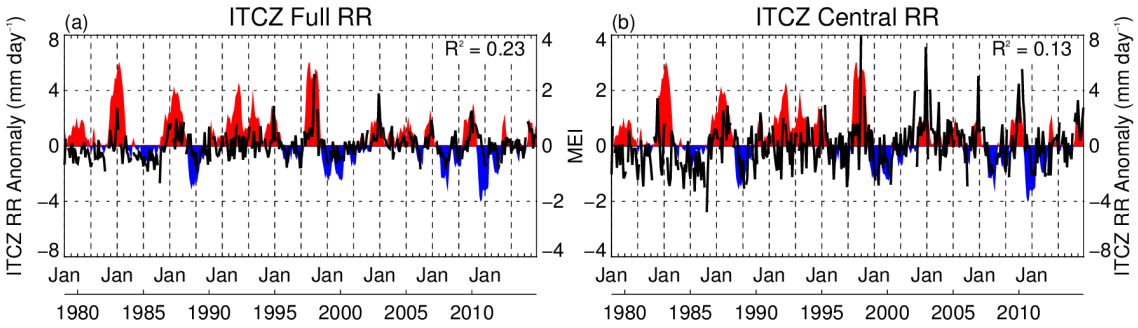

Figure 3.15: MEI (color) and ITCZ RR anomalies (black) for the (a) full ITCZ latitude and (b) central ITCZ. R^2 values are shown in the upper right corner of each plot.

The ENSO signal is removed using a method similar to Bain et al. (2011), with anomalies of ITCZ latitudes and extents regressed against the MEI for months when the MEI is greater then 0.5 or less than -0.5. The anomalies predicted by the regressions are then subtracted from the anomalies derived after the removal of the mean annual cycle. An example of ENSO signal removal for monthly ITCZ width anomalies is shown in Figure 3.16. It is clear from Figure 3.16b that the negative trend in ITCZ width is reduced; however, the trend does remain negative after ENSO removal, with both Figures 3.16a-b indicating that only the largest of anomalies are removed from the data. This method of ENSO signal removal was performed for

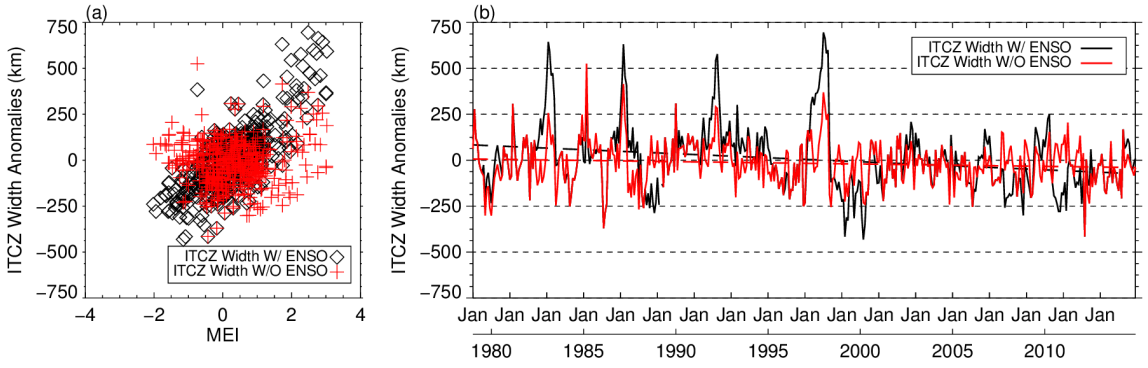

Figure 3.16: (a) Scatter plot of monthly ITCZ width anomalies before (black diamond) and after (red plus) the signal is removed. (b) Time series of monthly mean ITCZ widths before (black) and after (red) the ENSO signal is removed. Trends in ITCZ width are plotted as dashed lines.

all time series plots found in Sections 3.2 and 3.4. Although removal of the signal reduced the significance of trends in ITCZ characteristics, the sign of the trends did not change. This result is similar to that of Bain et al. (2011) who found that removing the ENSO signal from ITCZ latitudes and areas resulted in no significant trends. Zhou et al. (2011) found that removal of the ENSO signal through regression of anomalies to the Niño 3.4 index had little to no impact on the significance of trends in their data. Regression of the current climatology to the Niño 3.4 index produced results similar to both the MEI regression discussed above and Zhou et al. (2011). Because the overall trends in the results do not change and the ITCZ as a system is shaped by its environment, the ENSO signal was not removed here.

3.4 Seasonal Trends in ITCZ Characteristics

The mean annual cycle of all the ITCZ characteristics over the entire longitudinal extent of the Pacific ITCZ derived from both GPCP (solid) and TMI (dashed) RRs are presented in Figure 3.17. The ITCZ reaches its southern most latitude in March

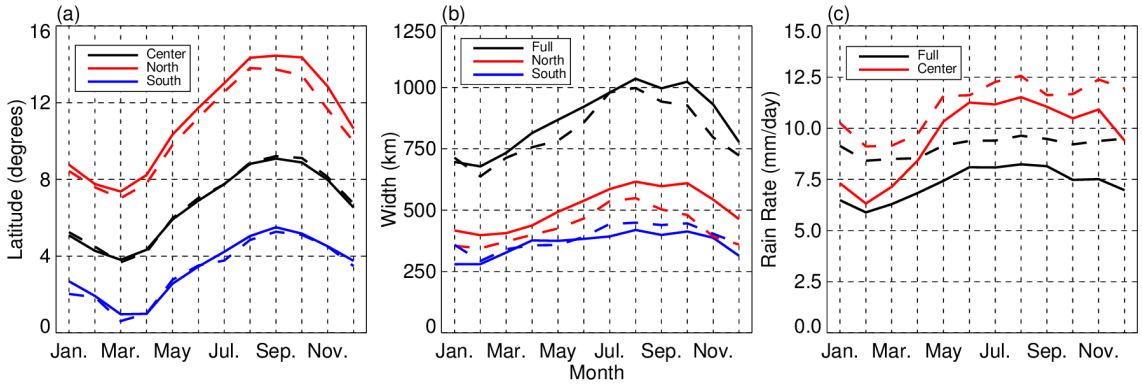

Figure 3.17: Mean annual cycle of ITCZ (a) latitudes, (b) extents, and (c) RRs with colors corresponding to different locations. Solid lines are represent GPCP derived values and dashed lines represent TMI derived values.

and its northern most latitude in September, indicating that the migration of the ITCZ throughout the year lags behind the peak in solar insolation by approximately two months. This result is similar to the findings of Waliser and Gautier (1993). The northern and southern boundaries follow the same cycle as the central latitude, but the location of the northern boundary has a larger range ($\sim 7°$) than the southern boundary ($\sim 5°$). These differences in boundary locations translate to differences in the northern and southern extents of the ITCZ (Figure 3.17b). Figure 3.17c shows the annual cycle of RRs for the full and central ITCZ. As with the latitude and width cycles, RR also lags the peak in solar insolation, but only by a month. In February, RRs for the full ITCZ are nearly identical to that of RRs near the center with differences becoming larger until June. The similarity between central and full ITCZ RRs in February is likely due to the $\pm 1°$ distance from the center containing a larger fraction of the total ITCZ width than in other months based on the changes in ITCZ width in Figure 3.17b. From June until September, RRs change very little, with RRs decreasing from September until February. Similar to the findings of Waliser and Gautier (1993), this indicates that convection in the ITCZ is strongest in boreal

summer and fall.

3.4.1 ITCZ Seasonal Latitudes

The total number of months that the ITCZ center, northern and southern boundary identifications are present in a given $2.5° \times 2.5°$ grid box are shown for each season in Figure 3.18. In DJF the northern boundary (Figure 3.18a) exhibits a large amount of variability from the dateline to $\sim 110°$W, with the boundary extending to almost 20°N. The northern boundary is much more linear in MAM (Figure 3.18d), although

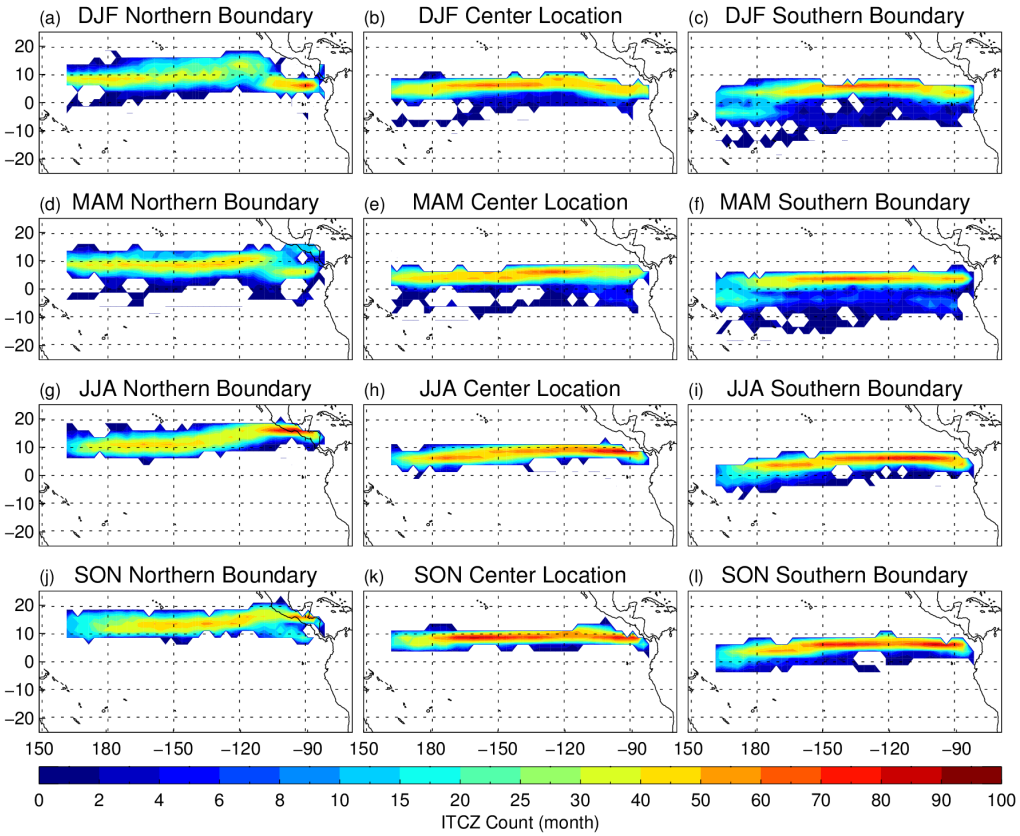

Figure 3.18: As in Figure 3.4, but for counts of ITCZ identification separated into seasons (rows). Northern boundary, center, and southern boundary are located in the first, second, and third columns, respectively.

there is still almost 10° range in locations. In JJA (Figure 3.18g), the boundary exhibits a distinct northward skew east of $\sim$ 130°W. This may be due to hurricane activity in these months increasing RRs off the west coast of the Americas, causing RRs to fall below the RR threshold in the boundary identification algorithm farther north. The northern boundary in SON (Figure 3.18j) has a similar distribution to MAM, but the boundary is farther north overall due to the ITCZ following changes in solar insulation. The center location of the ITCZ (middle column Figure 3.18) is mainly linear in all seasons with a range of $\sim$ 10° in location. For the southern boundary, DJF (Figure 3.18c) and MAM (Figure 3.18f) both show signs of double ITCZ influence, with about 5-10 months where boundary identifications are south of the equator in the EPAC. Although the identification algorithm is able to differentiate between northern and southern ITCZs, it is not perfect, with the total error of the algorithm shown in these seasons. JJA (Figure 3.18i) and SON (Figure 3.18l) are very similar with the majority of boundary identifications north of the equator over almost the entire longitudinal extent of the ITCZ. The southern boundary does cross the equator in the CPAC in JJA and SON, but this is most likely due to the influence of warm pool convection on RRs.

Seasonal time series of the center, northern and southern boundary latitudes of the ITCZ (solid) and their trends (dashed) are shown in Figure 3.19, with trends in Table 3.8. The values were derived over the ITCZ's entire longitudinal extent. The DJF season (Figure 3.19a) has the largest trends and is also the only season where the entire ITCZ has migrated in the same direction; northward. In all other seasons, the northern and southern boundaries migrate in opposite directions, with the northern (southern) boundary migrating southward (northward). JJA (Figure 3.19c) has some of the weakest trends, suggesting that changes in ITCZ latitude tend to occur during boreal winter. It is worth noting that only one of the trends are

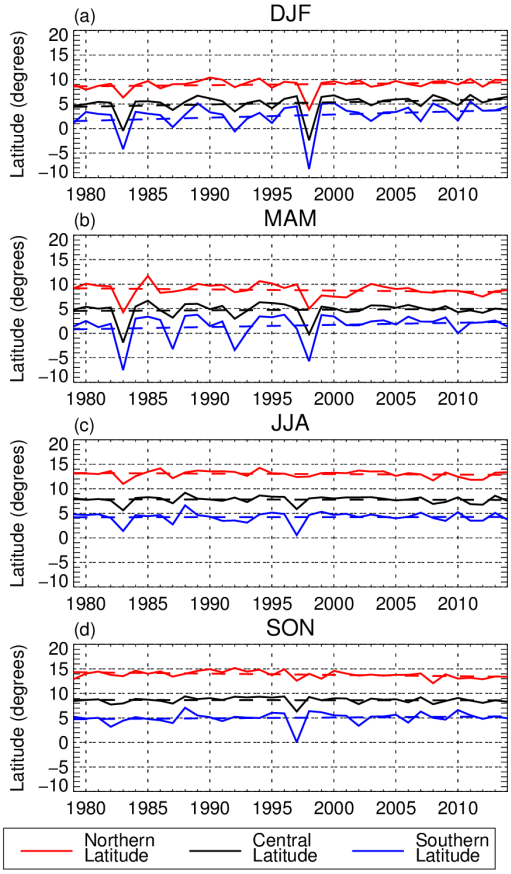

Figure 3.19: Time series of seasonal ITCZ latitudes (solid) and trends (dashed) over the entire longitudinal extent of the ITCZ. Trends are found in Table 3.8.

Table 3.8: Trends for seasonal ITCZ latitudes in Fig. 3.19. Trends have units degrees decade^{-1}. Italics represents confidence level greater than 90%; boldface confidence level greater than 95%.

Season	Center Latitude	Northern Boundary	Southern Boundary
DJF	0.445	0.237	0.644
MAM	0.126	-0.221	0.437
JJA	-0.033	-0.104	0.012
SON	-0.028	**-0.265**	0.164

significant (95% confidence level, Table 3.8). The seasonal ITCZ latitude anomalies are further separated into the CPAC and EPAC in Figure 3.20.

In the CPAC (Figures 3.20a-d), trends in latitude tend to be the same sign as those calculated over the entire longitudinal extent (Figure 3.19), but the magnitude of the trends are much different (Table 3.9). In DJF (Figure 3.20a), the entire

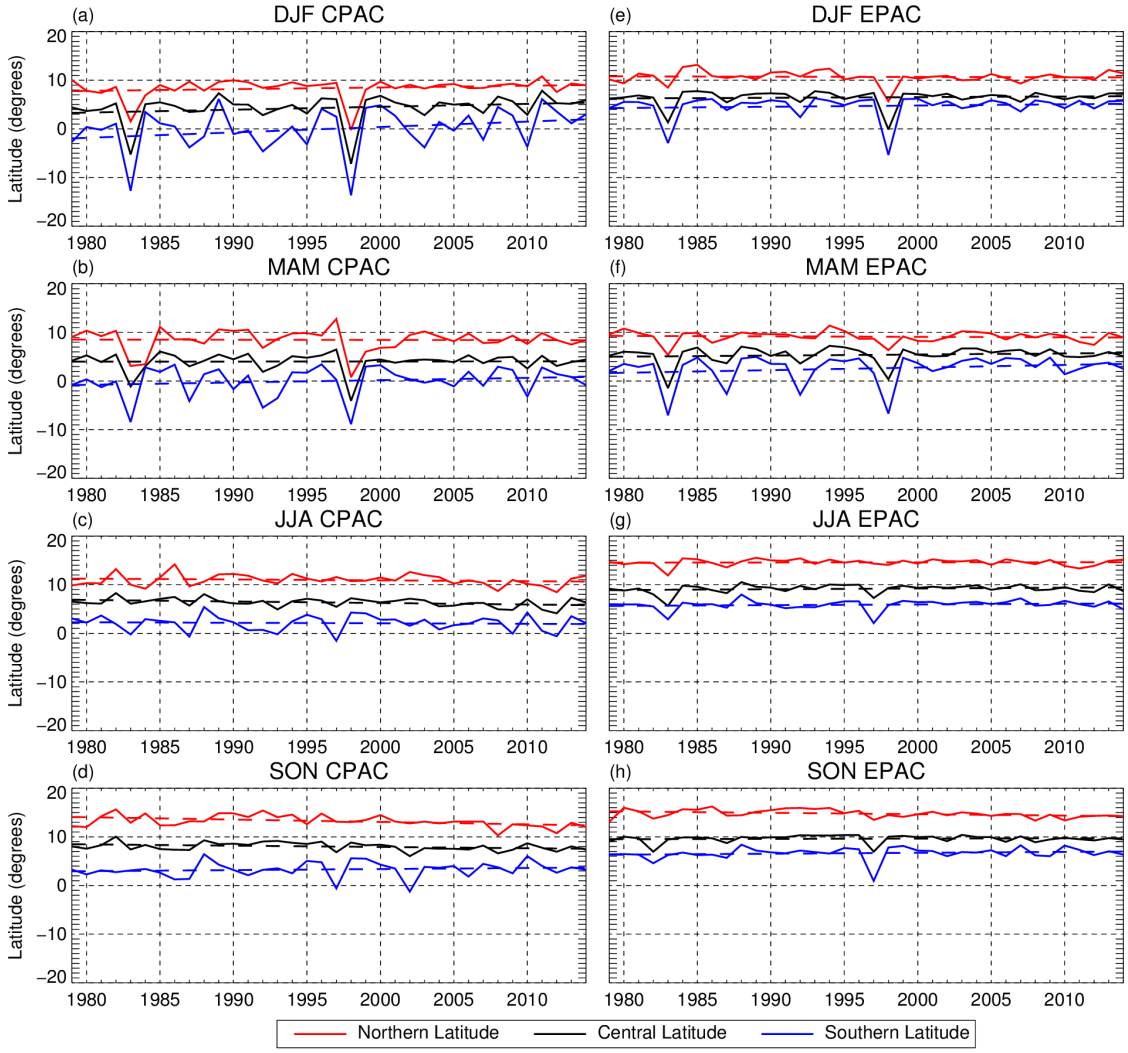

Figure 3.20: Monthly latitude anomalies for the central, northern, and southern latitudes of the ITCZ in the (a-c) Central and (d-f) Eastern Pacific. Trends are found in Table 3.9

Table 3.9: Trends for Seasonal ITCZ latitudes in Fig. 3.20. Trends have units degrees decade^{-1}. Italics represents confidence level greater than 90%; boldface confidence level greater than 95%.

	Center Latitude		Northern Boundary		Southern Boundary	
Season	CPAC	EPAC	CPAC	EPAC	CPAC	EPAC
DJF	0.408	0.127	0.100	-0.052	0.900	0.252
MAM	0.029	0.211	-0.027	-0.139	0.485	0.551
JJA	-0.313	0.154	-0.175	0.024	-0.103	0.142
SON	-0.265	0.058	*-0.489*	-0.284	0.215	0.187

ITCZ (i.e., the center and boundaries) migrated northward, while during JJA (Figure 3.20c) the ITCZ did the opposite, migrating southward. MAM (Figure 3.20b) and SON (Figure 3.20d) are similar in that the northern and southern boundaries migrated toward the center of the ITCZ; however, the center of the ITCZ migrated in different directions in each season, with a weak southward trend in MAM and a strong northward trend in SON.

Trends in the EPAC (Figures 3.20e-h) are a little more consistent, with ITCZ centers and southern boundaries migrating northward in all seasons. Differences only appear in JJA (Figure 3.20f), where the northern boundary migrates northward whereas all other months show the northern boundary migrating southward. This difference indicates a northward migration of the entire ITCZ, making the changes in JJA in the EPAC opposite of the changes seen in the CPAC.

3.4.2 ITCZ Seasonal Widths

Seasonal mean ITCZ widths over the longitudinal extent of the ITCZ are shown in Figure 3.21 with trends in Table 3.10. As expected from the seasonal latitude analysis above, most seasons do not exhibit significant trends in ITCZ width (Table 3.10); however, all trends in all seasons are negative. MAM (Figure 3.21b) saw the

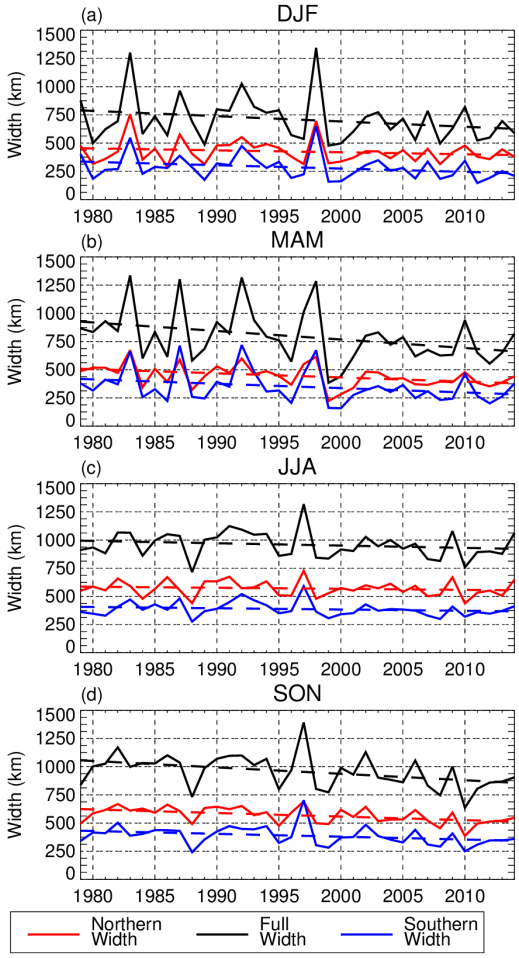

Figure 3.21: As in Figure 3.19 but for width. Trends are found in Table 3.10.

Table 3.10: Trends for seasonal ITCZ widths in Fig. 3.21. Trends have units km decade^{-1}. Italics represents confidence level greater than 90%; boldface confidence level greater than 95%.

Season	Full Width	Northern Width	Southern Width
DJF	-43.618	-23.214	-20.403
MAM	-71.569	*-37.692*	-33.877
JJA	-12.980	-8.098	-4.882
SON	*-47.771*	**-26.463**	-21.308

largest decrease in ITCZ width, with a 258 km reduction in the past 36 years. SON (Figure 3.21d) and DJF (Figure 3.21a) came in second and third, with reductions of 172 km and 157 km, respectively. As previously stated, JJA had the smallest decrease in ITCZ width at only 47 km. Based on the trends in the northern and southern extents, the reduction in ITCZ width was mostly symmetric, with a slightly larger reduction in the northern extent in all seasons. An interesting feature of Figure 3.21 is that while an ENSO signal is present, it tends to appear predominantly in DJF and MAM, with only the large El Niños of 1982/1983 and 1997/1998 in JJA and SON. This is due to El Niño occurring predominantly during boreal fall and winter.

Figure 3.22 separates width trends into the CPAC and EPAC for all four seasons with trends in Table 3.11. In the CPAC (Figures 3.22a-d) the full ITCZ width shows narrowing trends in all seasons. Both the northern and southern extents tend to co-vary, with very similar values indicating symmetry in the CPAC ITCZ. The large, periodic peaks in all seasons align closely with ENSO events, suggesting a strong ENSO influence in this region. The EPAC shows a similar picture (Figures 3.22e-h), but overall trends are weaker than in the CPAC.

Table 3.11: Trends for seasonal ITCZ widths in Fig. 3.22. Trends have units km decade^{-1}. Italics represents confidence level greater than 90%; boldface confidence level greater than 95%.

Season	Full Width		Northern Width		Southern Width	
	CPAC	EPAC	CPAC	EPAC	CPAC	EPAC
DJF	-85.433	-34.835	-33.332	-21.953	-52.101	-12.882
MAM	-59.535	-75.415	-7.487	-38.116	-52.048	-37.299
JJA	-7.784	-13.273	15.032	-14.622	-22.817	1.349
SON	-78.476	-52.544	-25.007	**-37.831**	-53.469	-14.713

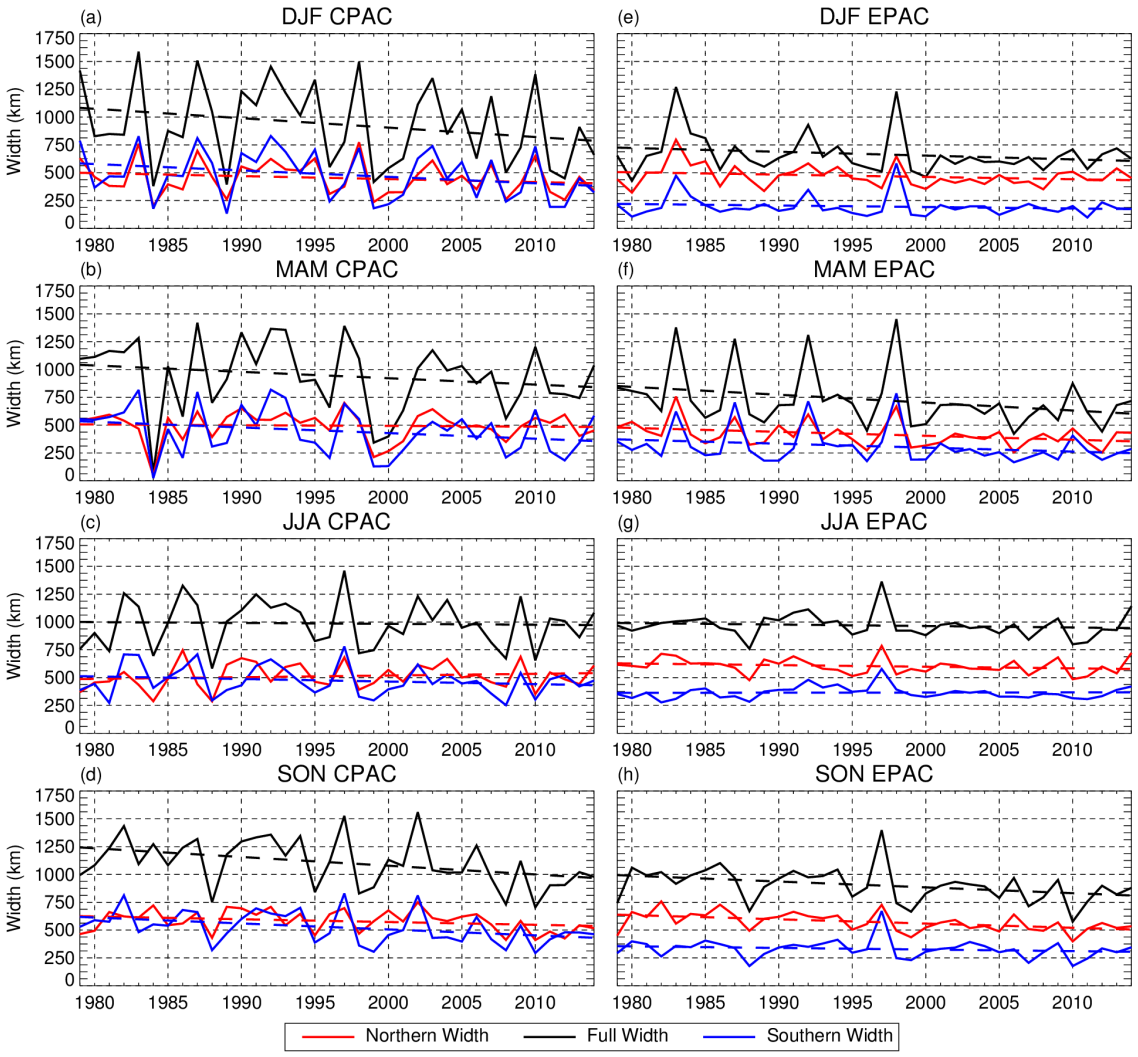

Figure 3.22: As in Figure 3.20 but for width. Trends are found in Table 3.11.

Based on the northern and southern extents, the ITCZ is mainly asymmetric in the EPAC, with the northern extent roughly twice as wide as the southern extent in all seasons but MAM (Figure 3.22f). An interesting feature in the EPAC is that the two large El Niño events of 1982/1983 and 1997/1998 appear in the DJF (Figure 3.22e) time series, but the events of 1987 and 1992 are almost nonexistent. However, all four of these events are clearly visible in the MAM (Figure 3.22f) time series,

showing the delayed impact of ENSO events in the EPAC domain. As previously mentioned for the long-term time series, many of the seasons in both domains (namely DJF and MAM) appear to be less variable after 1998. It is worth noting that only the trend in the northern width of the ITCZ in the EPAC is significant at a 90% confidence level.

3.4.3 ITCZ Seasonal Rain Rates

ITCZ seasonal RRs over the entire longitudinal extent of the ITCZ are shown in Figure 3.23 for both the full ITCZ RR (black) and the central ITCZ RR (red),

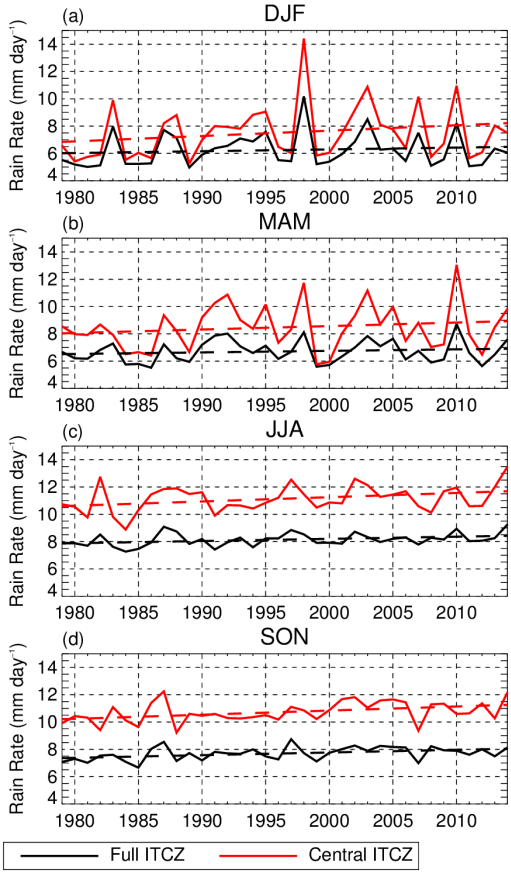

Figure 3.23: As in Figure 3.19 but for RR. Trends are found in Table 3.12.

Table 3.12: Trends for seasonal ITCZ RRs in Fig. 3.23. Trends have units mm day^{-1} decade^{-1}. Italics represents confidence level greater than 90%; boldface confidence level greater than 95%.

Season	Full ITCZ RR	Central ITCZ RR
DJF	0.132	0.434
MAM	0.112	0.256
JJA	0.159	0.297
SON	*0.196*	*0.255*

with trend values in Table 3.12. The strongest trends in ITCZ RR are over the central region of the ITCZ, as was shown in Figure 3.12, with the largest trend in DJF (Figure 3.23a). This is interesting because RRs over the full ITCZ have strengthened the most during JJA (Figure 3.23c) and SON (Figure 3.23d), while RRs over the full ITCZ for DJF are the second weakest, indicating that RR trends outside of the central ITCZ must be weak or even slightly negative. Trends over the central ITCZ in MAM, JJA, and SON are similar with increases of roughly 1 mm day^{-1} over the past 36 years.

Seasonal ITCZ RR intensity near the center and over the full ITCZ for the CPAC and EPAC is shown in Figure 3.24 with trends in Table 3.13. The CPAC region (Figures 3.24a-d) has considerable variability in trends between seasons and between the center and full width of the ITCZ. For example, in DJF (Figure 3.24a) RRs over the full ITCZ in the CPAC indicate slight weakening in precipitation intensity while RRs near the center of the ITCZ indicate strengthening. MAM (Figure 3.24b) shows similar features for the full ITCZ, but RRs near the center of the ITCZ exhibit slight weakening.

Although none of the aforementioned trends are significant, it is likely that ENSO is impacting results in these seasons in the CPAC. It is worth noting that there

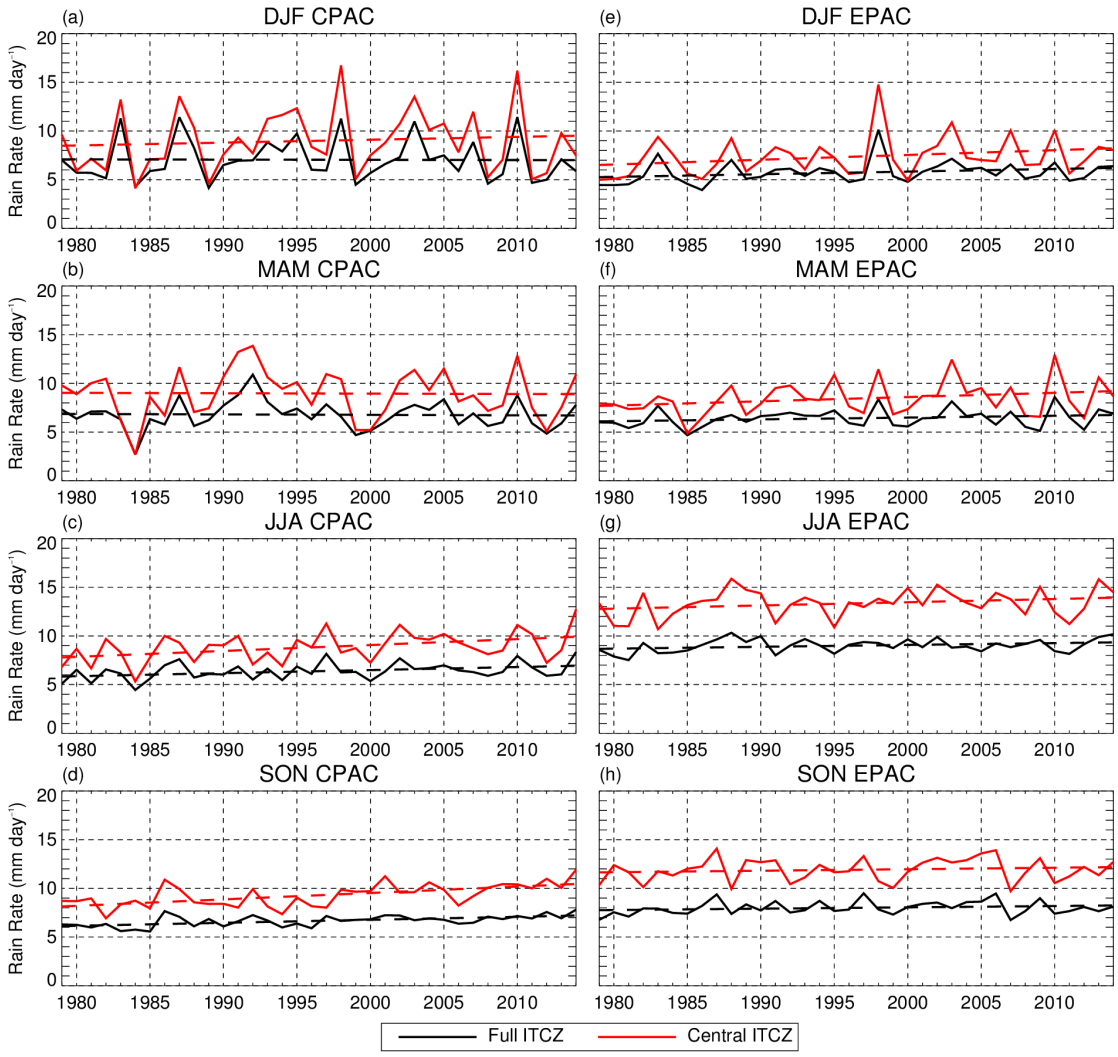

Figure 3.24: As in Figure 3.20 but for RR. Trends are found in Table 3.13.

are a few seasons near the beginning of the DJF and MAM time series where the ITCZ is quite narrow (2°-wide or less), which makes the center ITCZ (±1° from the ITCZ center latitude) the same size as the full ITCZ. In JJA (Figure 3.24c) and SON (Figure 3.24d), RR trends in the full ITCZ and near the center ITCZ indicate significant strengthening, with RRs near the center of the ITCZ increasing at twice the rate of the full ITCZ (Table 3.13).

Table 3.13: Trends For Seasonal ITCZ RRs in Fig. 3.24. Trend has units mm day^{-1} decade^{-1}. Italics represents confidence level greater than 90%; boldface confidence level greater than 95%.

Season	Full ITCZ RR		Central ITCZ RR	
	CPAC	EPAC	CPAC	EPAC
DJF	-0.023	0.271	0.309	0.561
MAM	-0.046	0.186	-0.017	0.448
JJA	0.314	0.190	*0.694*	0.352
SON	**0.309**	0.137	*0.627*	0.113

RR trends in the EPAC (Figures 3.24e-h) are less variables than in the CPAC with all trends showing increases in precipitation intensity. In DJF and MAM (Figures 3.24e-f), RRs over the full and near the center of the ITCZ have very similar values, with the largest differences occurring in ENSO years. These differences in RR between the full and center of the ITCZ were also shown in Figure 3.17; however, the trends in RRs near the center of the ITCZ are twice that of the full ITCZ (Table 3.13). RRs near the center of the ITCZ in JJA and SON also increase at twice the rate of the full ITCZ, but there are larger differences in RRs for the central and full ITCZ (Figures 3.24g-h).

4. SUMMARY AND DISCUSSION

This study combined ERA-Interim, and TMI and GPCP RRs to objectively identify the ITCZ and create a 36-year climatology of characteristics including center latitude, northern and southern extents, and rainfall intensity. The method outlined by Berry and Reeder (2014) was applied to monthly mean ERA-Interim data to identify the ITCZ center, with TMI and GPCP RRs used to locate ITCZ convection boundaries and calculate the extent of the ITCZ. RRs within ITCZ boundaries were then used to determine the intensity of ITCZ precipitation.

One advantage of the current algorithm over those used by Waliser and Gautier (1993) and Bain et al. (2011) is that it is objective and can be applied to any combination of gridded reanalysis and RR dataset or climate model output. Although the initial ITCZ identification is limited to model fields, application to any reanalysis or GCM currently available will produce self-consistent results, allowing for comparison of center locations between models (Berry and Reeder 2014). The use of gridded RR data is also advantageous as any currently available gridded RR dataset can be used in the algorithm with only minor adjustments for resolution or biases, as shown with the use of both TMI and GPCP RRs. It is also possible to apply the algorithm solely to model fields, allowing one to determine changes in ITCZs of GCMs. This direct measure of the ITCZ may help determine the relationship between changes in the ITCZ characteristics and the strength of the Hadley circulation.

As in previous studies (e.g., Waliser and Gautier 1993; Waliser and Somerville 1994; Bain et al. 2011) the ITCZ favors the northern hemisphere, with a preferred latitude of 8°N (Fig. 3.2a); however, there is a large amount of interannual variability in the location of the ITCZ (Fig. 3.5a), with the largest changes associated with

ENSO. The southern boundary of the ITCZ has a preferred latitude of 4°N, with the northern boundary much more variable with no apparent latitude preference. The extent of the ITCZ was highly variable with values ranging from 250 to 1500-km.

Changes in the location of the center and boundaries over the full longitudinal ITCZ and in the CPAC and EPAC were small, on the order of 1° in the past 36 years, with no trend statistically significant at the 90% level. This was not the case when changes in ITCZ extent were considered, with significant changes on the order of tens to hundreds of kilometers. These trends were observed in both the EPAC and over the entire ITCZ. What is most interesting about ITCZ width anomalies is that there appears to be less interannual variability in ITCZ extent after 1998. This shift is observed mainly in the EPAC and appears most prominently in DJF and MAM. This could be related to a shift in Pacific interdecadal variability (PDV), which was also observed by Gu and Adler (2013) in sea surface temperature, precipitation, and water vapor data.

Gu and Adler (2013) found decreases in both column water vapor and precipitation on the northern and southern boundaries of the ITCZ (their Fig. 9) were attributed to the components of sea surface temperature anomalies related to PDV. However, combining the effects of the PDV and surface warming Gu and Adler (2013; their Fig. 10) showed a nearly symmetric decrease in precipitation around the CPAC ITCZ region, but an asymmetric response in the EPAC, with precipitation decrease (increases) on the northern (southern) side. The apparent reduction of interannual variability in ITCZ characteristics after 1998 in the present study, which are located predominantly in the EPAC, may be a result of these offsetting effects in the EPAC working in opposite directions on the northern and southern ITCZ edges. In addition, the results here indicate that the reduced interannual variability in tropical mean precipitation after the shift shown by other studies is driven by changes in the

extent of deep convection in the ITCZ, rather than the intensity or characteristics of the deep convection, as the intensity of the rain in the ITCZ band does not show a corresponding shift in interannual variability.

Trends in the seasonal latitudes of the ITCZ, although weak, were stronger than the long-term trends. Seasonal trends of ITCZ widths showed contraction in all months in the CPAC with large ENSO signals in DJF and MAM. Trends in the EPAC were similar, but weaker, with a prominent ENSO signal mainly in MAM due to the time it takes for ENSO to propagate to the eastern Pacific Ocean. These weaker trends in the EPAC also caused trends calculated over the full longitudinal extent to be weaker. The northern and southern ITCZ extents in the CPAC were symmetric, whereas the EPAC is very asymmetric in all seasons except MAM. This asymmetry maybe partly a result of RR biases between the GPCP and TMI datasets, as regridded TMI RRs still produce asymmetries, but not nearly as large. It is also worth noting that the lack of SSM/I data in the GPCP before 1987, which was found to create inhomogeneities in time series (Section 2.2), did not create any discontinuities in the time series of ITCZ characteristics (Figure 3.5), indicating little influence on the results of the present study.

Over the past 36 years the ITCZ has narrowed and precipitation has intensified, with precipitation near the center of the ITCZ increasing faster than over the entire ITCZ. The narrowing of the ITCZ observed in the current study is in contrast to widening trends in the global ITCZ observed by Zhou et al. (2011; their Figure 5). This suggests that the Pacific ITCZ is not responsible for the global ITCZ expansion. The increase in precipitation in areas with climatologically heavy rainfall has been coined the "rich-get-richer" mechanism. Zhou et al. (2011) and Lau et al. (2013) noted similar increases in GPCP RRs and the RRs of 14 CMIP5 models, respectively. However, neither of the studies directly measured changes in the char-

acteristics of convection that may be responsible for changes in the precipitation intensity of the ITCZ. Because RRs are related to the intensity of convection (Zipser 1994; Zipser and Lutz 1994; Petersen et al. 1996; Nesbitt et al. 2000), it is probable that convection in the ITCZ has become more intense and possibly deeper over this time period. This intensification may be influencing the observed strengthening of the Hadley circulation as more intense convection changes the latent heating profile that helps drive the circulation. Lau and Kim (2015) found evidence of such a link between the ITCZ and the Hadley circulation in 33 CMIP5 models where changes in the strength of the Hadley circulation were linked to a "deep-tropics squeeze" (DTS), which was marked by narrowing and deepening of the ITCZ. With the current study presenting observational evidence of a DTS and observationally based studies indicating a strengthening of the Hadley circulation (e.g., Hu and Fu 2007; Seidel et al. 2008; Hu et al. 2011), it is likely that changes in the ITCZ and the Hadley circulation are related. However, the mechanism forcing changes in the ITCZ is still unclear.

Neggers et al. (2007) proposed a possible forcing mechanism that is consistent with the observed changes in the ITCZ found in this study. Their work suggests that the transport of subtropical moisture may be responsible for changes in the ITCZ. Neggers et al. (2007) used a quasi-equilibrium tropical circulation model (QTCM) and found that modifying the moistening timescales of shallow convection controlled the transport of dry air into the tropics. This acted to suppress convection at the edges of the ITCZ, while a series of feedbacks led to enhancement of convection near the center of the ITCZ. This *shallow cumulus humidity throttle* could be responsible for the DTS observed by Lau and Kim (2015) and the narrowing and intensification of the ITCZ found here. Sohn and Park (2010) observed a similar mechanism when studying changes in the strength of the Hadley circulation through water vapor transport. Their results indicated that the Hadley circulation has strengthened,

with the subtropics becoming drier and the deep tropics becoming wetter due to increased subsidence and low-level moisture transport, respectively. While the long-term changes in width and intensity shown here are consistent with the idea of a narrowing and intensifying ITCZ possibly due to remote feedbacks with the subtropics, examination of co-variability in width and precipitation intensity at monthly timescales is contradictory.

Figure 4.1 shows monthly ITCZ widths as a function of full (Figure 4.1a) and central (Figure 4.1b) ITCZ RRs. This shows that RR tends to increase when the ITCZ is wider and decreases when the ITCZ is narrower. This indicates that either the RR may not fully capture changes in the intensity or characteristics of deep convection in the ITCZ or that the mechanisms that drive relationships between ITCZ width and intensity at different timescales are still not fully understood. This is discussed further in Section 4.2.

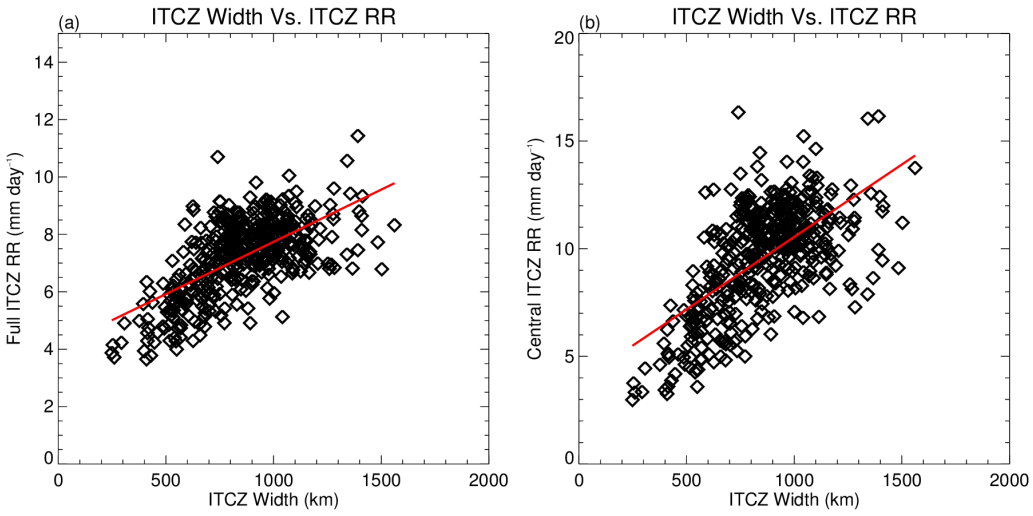

Figure 4.1: Monthly zonal mean ITCZ width (abscissa) and corresponding monthly mean ITCZ RR (ordinate) for the (a) full ITCZ RR and (b) central ITCZ RR.

4.1 Limitations

The method of ITCZ identification used in this study requires gridded variables, which are found only in reanalysis and GCM data, constraining the algorithm to these specific data sets. Although reanalyses are heavily constrained by observational data, model physics do influence the output, with data sparse regions, such as the tropical Pacific, reflecting the model more than data rich regions. An example of this was shown in the comparison of monthly ERA-Interim precipitation to GPCP by Dee et al. (2011, their Figure 26), with very similar precipitation over land and very different precipitation over ocean between the two data sets. Dee et al. (2011) attributed these differences to the lack of observations over the ocean, such as vertical profiles of temperature and humidity from radiosondes, with other variables such as wind also suffering from the lack of data. However, based on the results of Berry and Reeder (2014) and those shown here (i.e., good correspondence between observed RRs and the objective ITCZ identifications), these errors in the ERA-Interim likely do not have large impacts on ITCZ identification.

Another limitation of the identification algorithm is potential bias in the RR datasets. Although the GPCP and RSS RR datasets are considered high quality, they still contain errors due to limitations in satellite based RR estimates and the lack of in situ observations over the ocean. This is especially important to consider when remembering that passive microwave RR retrievals are less accurate at low RRs, which may be the cause of the differences between GPCP and TMI zonal mean RRs along the ITCZ edges shown in Figure 3.3. The resolution differences between data was also a challenge, with the higher resolution TMI data (relative to GPCP) containing high frequency variations in RR near ITCZ boundaries. Although smoothing was shown to reduce the noise and make the derived characteristics be-

tween TMI and GPCP more consistent, it effectively reduced to the resolution of the boundary identifications. Ensuring that other RR data sets produce similar results to those presented here is important to ensure that RR biases and resolution effects have been fully resolved.

The last major limitation of the ITCZ identification is the difficulty identifying the ITCZ boundaries in the west Pacific warm pool region. Although visual identification of the ITCZ can be difficult in this region, the simple RR threshold method used here is essentially useless in this region due to the heavy rainfall that is present in the warm pool. A more advanced method for identification is required for this region. The identification method was also not applied to the Atlantic and Indian oceans, and therefore, may not be applicable to those regions, although Berry and Reeder (2014) successfully used the method to identify the ITCZ center location around the globe over both land and ocean. However, Zhou et al. (2011) used a similar RR threshold to identify ITCZ boundaries in global zonal mean GPCP data with success, which indicates that the identification method from the present study is likely applicable to these regions.

4.2 Future Work

It is clear that there is still more work needed to understand the observed changes in the ITCZ and their links to the subtropics and the Hadley circulation. Application of the ITCZ identification and characterization algorithm presented in this study to GCMs in the future will provide a quantitative measure of the ITCZ simulated by the models and allow for better comparison with observed ITCZ characteristics. A more quantitative study of the intensity of the ITCZ PF characteristics is also needed. A brief study of changes in convection was performed by Tan et al. (2015), who found that the frequency of organized deep convection has increased in recent

decades within the ITCZ region with small scale unorganized convection decreasing near the edges of the ITCZ. However, the study did not examine changes in convective characteristics such as the structure or measures of convective intensity like the maximum height of the 30-dBZ echo or the maximum storm height. Thus, a more in-depth study of PF convective characteristics will provide a more complete understanding of the types and morphology of ITCZ convection and is necessary to determine the direct impacts changes in convection have on the ITCZ heating profile and the Hadley circulation.

As a first step, PFs from the TRMM RPF database located in the ITCZ boundaries are extracted on a monthly basis and the distance, in degrees, that each PF is from the center of the ITCZ is calculated. Using these data, all months where the monthly zonal mean ITCZ width is greater than or less than 1σ from the climato-

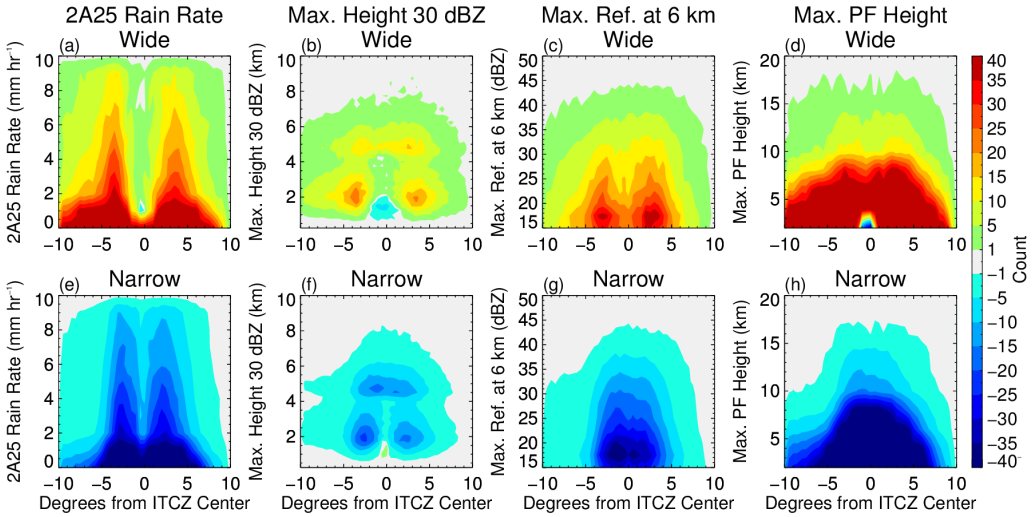

Figure 4.2: Mean monthly-anomalies of the number of PFs with a given characteristic at a given distance from the center of the ITCZ when (top) the zonal mean ITCZ width is 1 σ above the climatological mean ITCZ width and (bottom) the zonal mean ITCZ width is 1 σ below the climatological mean ITCZ width. (a,e), 2A25 RR, (b,f) maximum height reached by the 30-dBZ echo, (c,g) maximum reflectivity at 6 km, and (d,h) maximum height reached by the PF.

logical mean ITCZ width are used to examine changes in PFs between anomalously wide and narrow ITCZs. Figure 4.2 shows the anomalies of occurrence of PFs with certain convective characteristics during wide (top row) and narrow (bottom row) ITCZs. From Figure 4.2a, when the ITCZ is wider the number of PFs with RRs below 2 mm hr^{-1} increases by at least 40 for nearly all distances from the ITCZ center, except within $\pm 2^{\circ}$ of the ITCZ center. For PFs with RRs greater than 2 mm hr^{-1}, counts are roughly symmetric about the ITCZ center, with peak increases centered at 4°N/S and suggests that more intense precipitation occurs more often and farther from the ITCZ center during wide ITCZ months. It is interesting that counts for all RRs within $\pm 2^{\circ}$ of the ITCZ center increase only slightly, indicating essentially no change in frequency of PFs in this region. An opposite distribution of PF frequency anomalies is seen during narrow ITCZs (Figure 4.2e), meaning the frequency of precipitation decreases at all RRs in narrow ITCZ months. But, as in the wide ITCZ months, PF frequency close to the ITCZ center is not affected as much as PFs near ITCZ edges.

Figures 4.2b,f indicate that strong convection (i.e., 30 dBZ echos near 6 km) near the ITCZ center increases (decreases) frequency in wide (narrow) ITCZ months. This is less evident in the 6 km reflectivity histograms (Figures 4.2c,g); however, symmetrical changes in frequency similar to those in RR are observed in wide ITCZ anomalies. From Figures 4.2d,h both shallow and deep convection become more frequent for wide ITCZ months, with shallow convection (i.e., heights below 5 km) being most influenced. During narrow months, however, shallow convection is reduced the most, suggesting that deep convection remains during narrow ITCZ months. Although some of the conclusions drawn from Figure 4.2 may seem to contradict the idea that as the ITCZ narrows it becomes more intense, it is important to remember that Figure 4.2 simply shows the changes in frequency of PFs with given characteris-

tics and is not necessarily a measure of the overall convective intensity of the ITCZ, i.e., PF counts during narrow ITCZ months may simply be lower than average with no change to the distributions of PF intensity.

To better understand the changes in the intensity of ITCZ convection, PF convective characteristics were averaged over 0.5° bins based on their distance from the ITCZ center. Figure 4.3 shows these mean characteristics for wide (red), narrow (black), and all (black dashed) ITCZ widths. The characteristics are also separated by all PFs (bold colors) and deep convective PFs (light colors), defined as any PF with a maximum height over 9 km (Johnson et al. 1999). Although these plots do

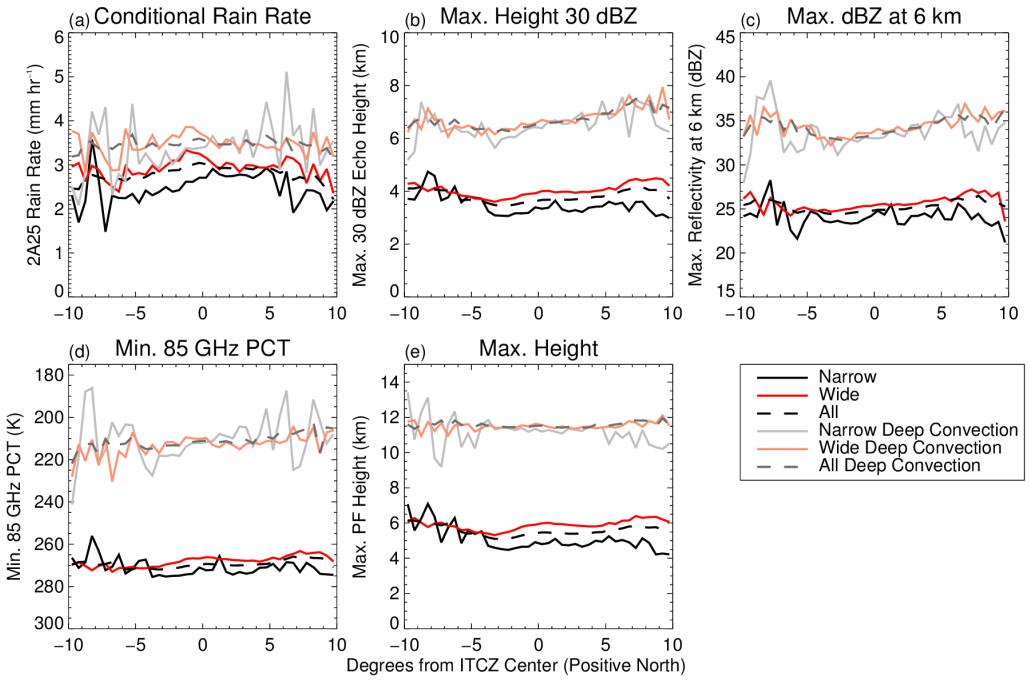

Figure 4.3: Mean PF characteristics at a given distance from the center of the ITCZ for (black) narrow ITCZ months, (red) wide ITCZ months, and (black dashed) all months. Characteristics include (a) conditional rain rate from 2A25, (b) maximum height of the 30-dBZ echo, (c) maximum dBZ at 6-km, (d), minimum 85 GHz PCT, and (e) maximum height reached by the feature. Bold colors represent values for all RPFs with light colors representing values for deep convection.

not have a Gaussian-type distribution as might be expected from zonal mean RR in Figure 3.3 (i.e., more intense convection near the center of the ITCZ), the conditional RRs (Figure 4.3a) do align with findings from Nesbitt et al. (2006). In their work Nesbitt et al. (2006) found that conditional RRs in the Pacific were nearly uniform over the ITCZ region (their Fig. 13). This was attributed to mesoscale convective systems (MCSs) near the boundaries of the ITCZ producing large RRs, causing the conditional RRs in these areas to be large. This also helps explain the shape of curves in other convective intensity parameters as MCSs contain intense convection. One interesting feature of all the characteristics in Figure 4.3 is that when all PFs (bold) are considered, the values for wide ITCZ months (black) tend to be higher than for all months, with narrow ITCZ months (red) falling below all months. This indicates that convection is weaker when the ITCZ is narrow (as was seen in Figure 4.1); however, more work must be done to better study variability in the distribution and morphology of convection in the ITCZ.

Although there are many implications of the present research, the main goal of future work is to use observational data to determine if the *shallow cumulus humidity throttle* mechanism discussed earlier is viable. Although Neggers et al. (2007) did find that their QTCM produced changes in the ITCZ when the moistening from subtropical shallow convection was changed, this has not been studied with observations. First, the relationship between shallow subtropical convection and subtropical moisture and moisture transport from the subtropics to the tropics must be quantified. The horizontal moisture fluxes can then be related to observed changes in the ITCZ characteristics observed here. Results from these future analyses may then be used to evaluate the ability of GCMs to capture this feedback mechanism and possibly help explain changes, or lack of thereof, in the Hadley circulation in GCMs.

5. CONCLUSIONS

An automated, objective ITCZ identification algorithm has been modified and applied to create a climatology of ITCZ characteristics, including ITCZ center, northern and southern boundary locations, extents, and precipitation intensity, from ERA-Interim variables and TMI and GPCP RRs. The algorithm can be run using any combination of gridded reanalysis, GCM, and RR data that provides the necessary variables, allowing to test not only the robustness of the algorithm to different input data, but to test the characteristics of the input data to each other. Climatological ITCZ characteristics derived here are consistent with previous works, suggesting that the method is valid.

Over the past 36 years, the Pacific ITCZ has narrowed 158 km and central ITCZ RRs have increased 1.1 mm day^{-1}. Separation of the ITCZ into CPAC and EPAC domains revealed larger changes in ITCZ characteristics in the CPAC than in the EPAC, while seasonal trend analysis showed the strongest changes occurred during boreal winter. A decrease in the interannual variability of ITCZ width was also identified and was linked to a shift in the PDV that has been studied in other works. A shift in variability was not shown in ITCZ RRs, which indicates that the width of the ITCZ, rather than its precipitation intensity, is related to the PDV. Initial analysis of RPFs located within ITCZ boundaries showed evidence of ITCZ convective intensification during anomalously wide ITCZ months; however, the robustness of these results was not clear from the brief analysis. Future research will use the identification and characterization method outlined here to study changes in the relationship between the ITCZ and subtropical moisture transport, which is thought to influence the width and intensity of the ITCZ.

REFERENCES

Adler, R. F., and R. A. Mack, 1984: Thunderstorm cloud height-rainfall rate relations for use with satellite rainfall estimation techniques. *J. Appl. Meteor.*, **23**, 280–296.

Adler, R. F., G. J. Huffman, A. Chang, R. Ferraro, P.-P. Xie, and Coauthors, 2003: The version-2 Global Precipitation Climatology Project (GPCP) monthly precipitation analysis (1979–present). *J. Hydrometeor.*, **4**, 1147–1167.

Ahrens, C. D., 2007: *Essentials of meteorology: an invitation to the atmosphere*. 5th ed., Cengage Learning, Belmont, CA, 504 pp.

Asnani, G., 1968: The equatorial cell in the general circulation. *J. Atmos. Sci.*, **25**, 133–134.

Back, L. E., and C. S. Bretherton, 2009: On the relationship between SST gradients, boundary layer winds, and convergence over the tropical oceans. *Journal of Climate*, **22**, 4182–4196.

Bain, C. L., J. De Paz, J. Kramer, G. Magnusdottir, P. Smyth, and Coauthors, 2011: Detecting the ITCZ in instantaneous satellite data using spatiotemporal statistical modeling: ITCZ climatology in the east Pacific. *J. Climate*, **24**, 216–230.

Bauer, P., J.-F. Mahfouf, W. S. Olson, F. S. Marzano, S. D. Michele, and Coauthors, 2002: Error analysis of TMI rainfall estimates over ocean for variational data assimilation. *Quart. J. Roy. Meteor. Soc.*, **128**, 2129–2144.

Bechtold, P., J.-P. Chaboureau, A. Beljaars, A. Betts, M. K ohler, and Coauthors, 2004: The simulation of the diurnal cycle of convective precipitation over land in a global model. *Quart. J. Roy. Meteor. Soc.*, **130**, 3119–3137.

Berrisford, P., P. Køallberg, S. Kobayashi, D. Dee, S. Uppala, and Coauthors, 2011: Atmospheric conservation properties in era-interim. *Quart. J. Roy. Meteor. Soc.*, **137**, 1381–1399.

Berry, G., and M. J. Reeder, 2014: Objective identification of the intertropical convergence zone: Climatology and trends from the ERA-Interim. *J. Climate*, **27**, 1894–1909.

Bjerknes, J., 1969: Atmospheric teleconnections from the equatorial pacific. *Monthly Weather Review*, **97**, 163–172.

Bjerknes, J., L. J. Allison, E. R. Kreins, F. A. Godshall, and G. Warnecke, 1969: Satellite mapping of the Pacific tropical cloudiness. *Bull. Amer. Meteor. Soc.*, **50**, 313–322.

Boucher, O., D. Randall, P. Artaxo, C. Bretherton, G. Feingold, and Coauthors, 2013: Clouds and aerosols. *Climate change 2013: the physical science basis. Contribution of Working Group I to the Fifth Assessment Report of the Intergovernmental Panel on Climate Change*, Cambridge University Press, 571–657.

Charney, J. G., 1971: Tropical cyclogenesis and the formation of the intertropical convergence zone. *Mathematical problems of geophysical fluid dynamics*, **13**, 355–368.

Chen, B., X. Lin, and J. T. Bacmeister, 2008: Frequency distribution of daily ITCZ patterns over the western-central Pacific. *J. Climate*, **21**, 4207–4222.

Cheng, C.-P., and R. A. Houze Jr., 1979: The distribution of convective and mesoscale precipitation in GATE radar echo patterns. *Mon. Wea. Rev.*, **107**, 1370–1381.

Dee, D., S. Uppala, A. Simmons, P. Berrisford, P. Poli, and Coauthors, 2011: The ERA-interim reanalysis: Configuration and performance of the data assimilation system. *Quart. J. Roy. Meteor. Soc.*, **137**, 553–597.

DeMoss, J. D., and K. P. Bowman, 2007: Changes in TRMM rainfall due to the orbit boost estimated from buoy rain gauge data. *J. Atmos. Oceanic Technol.*, **24**, 1598–1607.

DeMott, C. A., and S. A. Rutledge, 1998: The vertical structure of TOGA COARE convection. Part I: Radar echo distributions. *J. Atmos. Sci.*, **55**, 2730–2747.

Dodd, J., and I. James, 1997: The impact of latent-heat release on the Hadley circulation. *Quart. J. Roy. Meteor. Soc.*, **123**, 1763–1770.

Dorman, C. E., and R. H. Bourke, 1979: Precipitation over the Pacific Ocean, 30°S to 60°N. *Mon. Wea. Rev.*, **107**, 896–910.

Estoque, M., and M. Douglas, 1978: Structure of the intertropical convergence zone over the GATE area. *Tellus*, **30**, 55–61.

Fletcher, R. D., 1945: The general circulation of the tropical and equatorial atmosphere. *J. Meteor.*, **2**, 167–174.

Frank, W. M., 1983: The structure and energetics of the east Atlantic intertropical convergence zone. *J. Atmos. Sci.*, **40**, 1916–1929.

Garcia, O., 1985: *Atlas of highly reflective clouds for the global tropics: 1971-1983*. US Dept. of Commerce, National Oceanic and Atmospheric Administration, Environmental Research Laboratories, Washington, D.C.

Graham, N., and T. Barnett, 1987: Sea surface temperature, surface wind divergence, and convection over tropical oceans. *Science*, **238**, 657–659.

Griffith, C. G., W. L. Woodley, P. G. Grube, D. W. Martin, J. Stout, and Coauthors, 1978: Rain estimation from geosynchronous satellite imagery-visible and infrared studies. *Mon. Wea. Rev.*, **106**, 1153–1171.

Gruber, A., 1972: Fluctuations in the position of the ITCZ in the Atlantic and Pacific Oceans. *J. Atmos. Sci.*, **29**, 193–197.

Gu, G., and R. F. Adler, 2013: Interdecadal variability/long-term changes in global precipitation patterns during the past three decades: global warming and/or pacific decadal variability? *Clim. Dynam.*, **40**, 3009–3022.

Hack, J. J., W. H. Schubert, D. E. Stevens, and H.-C. Kuo, 1989: Response of the Hadley circulation to convective forcing in the ITCZ. *J. Atmos. Sci.*, **46**, 2957–2973.

Hilburn, K. A., and F. J. Wentz, 2008: Intercalibrated passive microwave rain products from the Unified Microwave Ocean Retrieval Algorithm (UMORA). *J. Appl. Meteor. Climatol.*, **47**, 778–794.

Holton, J. R., J. M. Wallace, and J. Young, 1971: On boundary layer dynamics and the ITCZ. *J. Atmos. Sci.*, **28**, 275–280.

Hou, A. Y., and R. S. Lindzen, 1992: The influence of concentrated heating on the Hadley circulation. *J. Atmos. Sci.*, **49**, 1233–1241.

Hu, Y., and Q. Fu, 2007: Observed poleward expansion of the Hadley circulation since 1979. *Atmos. Chem. Phys.*, **7**, 5229–5236.

Hu, Y., D. Li, and J. Liu, 2007: Abrupt seasonal variation of the ITCZ and the Hadley circulation. *Geophys. Res. Lett.*, **34**.

Hu, Y., C. Zhou, and J. Liu, 2011: Observational evidence for poleward expansion of the Hadley circulation. *Adv. Atmos. Sci.*, **28**, 33–44, doi:10.1007/s00376-010-0032-1.

Hubert, L. F., A. F. Krueger, and J. S. Winston, 1969: The double intertropical convergence zone-fact or fiction? *J. Atmos. Sci.*, **26**, 771–773.

Huffman, G. J., R. F. Adler, D. T. Bolvin, and G. Gu, 2009: Improving the global precipitation record: GPCP version 2.1. *Geophys. Res. Lett.*, **36**.

Iguchi, T., T. Kozu, R. Meneghini, J. Awaka, and K. Okamoto, 2000: Rain-profiling algorithm for the TRMM precipitation radar. *J. Appl. Meteor.*, **39**, 2038–2052.

Johnson, R. H., T. M. Rickenbach, S. A. Rutledge, P. E. Ciesielski, and W. H. Schubert, 1999: Trimodal characteristics of tropical convection. *J. Climate*, **94**, 2397–2418.

Kumar, A., F. Yang, L. Goddard, and S. Schubert, 2004: Differing trends in the tropical surface temperatures and precipitation over land and oceans. *J. Climate*, **17**, 653–664.

Kummerow, C., W. Barnes, T. Kozu, J. Shiue, and J. Simpson, 1998: The tropical rainfall measuring mission (TRMM) sensor package. *J. Atmos. Oceanic Technol.*, **15**, 809–817.

Kummerow, C., W. S. Olson, and L. Giglio, 1996: A simplified scheme for obtaining precipitation and vertical hydrometeor profiles from passive microwave sensors. *IEEE Trans. Geosci. Remote Sens.*, **34**, 1213–1232.

Lau, K.-M., and H.-T. Wu, 2007: Detecting trends in tropical rainfall characteristics, 1979–2003. *International Journal of Climatology*, **27**, 979–988.

Lau, K.-M., and H.-T. Wu, 2011: Climatology and changes in tropical oceanic rainfall characteristics inferred from Tropical Rainfall Measuring Mission (TRMM) data (1998–2009). *J. Geophys. Res.*, **116**.

Lau, W. K., and K.-M. Kim, 2015: Robust Hadley circulation changes and increasing global dryness due to CO_2 warming from CMIP5 model projections. *Proceedings of the National Academy of Sciences*, **112**, 3630–3635.

Lau, W. K.-M., H.-T. Wu, and K.-M. Kim, 2013: A canonical response of precipitation characteristics to global warming from CMIP5 models. *Geophys. Res. Lett.*, **40**, 3163–3169.

Leary, C. A., 1984: Precipitation structure of the cloud clusters in a tropical easterly wave. *Mon. Wea. Rev.*, **112**, 313–325.

Leith, C., 1973: The standard error of time-average estimates of climatic means. *J. Appl. Meteor.*, **12**, 1066–1069.

Lindzen, R. S., and A. V. Hou, 1988: Hadley circulations for zonally averaged heating centered off the equator. *J. Atmos. Sci.*, **45**, 2416–2427.

Liu, C., 2007: University of Utah TRMM precipitation and cloud feature database description version 1.0.

Liu, C., E. J. Zipser, D. J. Cecil, S. W. Nesbitt, and S. Sherwood, 2008: A cloud and precipitation feature database from nine years of TRMM observations. *J. Appl. Meteor. Climatol.*, **47**, 2712–2728.

Lu, J., G. A. Vecchi, and T. Reichler, 2007: Expansion of the Hadley cell under global warming. *Geophys. Res. Lett.*, **34**.

Mitas, C. M., and A. Clement, 2005: Has the Hadley cell been strengthening in recent decades? *Geophys. Res. Lett.*, **32**.

Mitas, C. M., and A. Clement, 2006: Recent behavior of the Hadley cell and tropical thermodynamics in climate models and reanalyses. *Geophys. Res. Lett.*, **33**, L01 810.

Mitchell, T. P., and J. M. Wallace, 1992: The annual cycle in equatorial convection and sea surface temperature. *J. Climate*, **5**, 1140–1156.

Neggers, R. A., J. D. Neelin, and B. Stevens, 2007: Impact mechanisms of shallow cumulus convection on tropical climate dynamics*. *J. Climate*, **20**, 2623–2642.

Nesbitt, S. W., R. Cifelli, and S. A. Rutledge, 2006: Storm morphology and rainfall characteristics of TRMM precipitation features. *Mon. Wea. Rev.*, **134**, 2702–2721.

Nesbitt, S. W., E. J. Zipser, and D. J. Cecil, 2000: A census of precipitation features in the tropics using TRMM: Radar, ice scattering, and lightning observation. *J. Climate*, **13**, 4087–4106.

Nguyen, H., A. Evans, C. Lucas, I. Smith, and B. Timbal, 2013: The Hadley circulation in reanalyses: Climatology, variability, and change. *J. Climate*, **26**, 3357–3376.

Oueslati, B., and G. Bellon, 2013: Convective entrainment and large-scale organization of tropical precipitation: Sensitivity of the CNRM-CM5 hierarchy of models. *J. Climate*, **26**, 2931–2946.

Petersen, W. A., S. A. Rutledge, and R. E. Orville, 1996: Cloud-to-ground lightning observations from TOGA COARE: Selected results and lightning location algorithms. *Mon. Wea. Rev.*, **124**, 602–620.

Pike, A. C., 1971: The inter-tropical convergence zone studied with an interacting atmosphere and ocean model. *Mon. Wea. Rev.*, **99**, 469–477.

Quan, X.-W., H. F. Diaz, and M. P. Hoerling, 2004: Change in the tropical Hadley cell since 1950. *The Hadley Circulation: Present, Past, and Future*, H. F. Diaz, and R. S. Bradley, Eds., Kluwer Academic Publisher.

Riehl, H., and J. S. Malkus, 1958: On the heat balance in the equatorial trough zone. *Geophysica*, **6**, 503–538.

Rienecker, M. M., M. J. Suarez, R. Gelaro, R. Todling, J. Bacmeister, and Coauthors, 2011: MERRA: NASA's modern-era retrospective analysis for research and applications. *J. Climate*, **24**, 3624–3648.

Seidel, D. J., Q. Fu, W. J. Randel, and T. J. Reichler, 2008: Widening of the tropical belt in a changing climate. *Nat. Geosci.*, **1**, 21–24.

Shin, D.-B., and L. S. Chiu, 2008: Effects of TRMM boost on oceanic rainfall estimates based on microwave emission brightness temperature histograms (METH). *J. Atmos. Oceanic Technol.*, **25**, 1888–1893.

Short, D. A., P. A. Kucera, B. S. Ferrier, J. C. Gerlach, S. A. Rutledge, and Coauthors, 1997: Shipboard radar rainfall patterns within the TOGA COARE IFA. *Bull. Amer. Meteor. Soc.*, **78**, 2817–2836.

Short, D. A., and K. Nakamura, 2010: Effect of TRMM orbit boost on radar reflectivity distributions. *J. Atmos. Oceanic Technol.*, **27**, 1247–1254.

Simpson, J., R. F. Adler, and G. R. North, 1988: A proposed tropical rainfall measuring mission (TRMM) satellite. *Bull. Amer. Meteor. Soc.*, **69**, 278–295.

Sohn, B., and S.-C. Park, 2010: Strengthened tropical circulations in past three decades inferred from water vapor transport. *J. Geophys. Res.*, **115**.

Stachnik, J. P., and C. Schumacher, 2011: A comparison of the Hadley circulation in modern reanalyses. *J. Geophys. Res.*, **116**.

Tan, J., C. Jakob, W. B. Rossow, and G. Tselioudis, 2015: Increases in tropical rainfall driven by changes in frequency of organized deep convection. *Nature*, **519**, 451–454.

Tao, W., E. Smith, R. Adler, A. Hou, R. Meneghini, and Coauthors, 2006: Retrieval of latent heating from TRMM measurements. *Bull. Amer. Meteor. Soc.*, **87**, 1555–1572.

Waliser, D. E., and C. Gautier, 1993: A satellite-derived climatology of the ITCZ. *J. Climate*, **6**, 2162–2174.

Waliser, D. E., and R. C. J. Somerville, 1994: Preferred latitudes of the intertropical convergence zone. *J. Atmos. Sci.*, **51**, 1619–1639.

Walker, C. C., and T. Schneider, 2005: Response of idealized Hadley circulations to seasonally varying heating. *Geophys. Res. Lett.*, **32**.

Wang, C.-c., and G. Magnusdottir, 2006: The ITCZ in the central and eastern Pacific on synoptic time scales. *Mon. Wea. Rev.*, **134**, 1405–1421.

Webster, P. J., 2004: The elementary Hadley circulation. *The Hadley Circulation: Present, Past, and Future*, H. F. Diaz, and R. S. Bradley, Eds., Kluwer Academic Publisher.

Wentz, F. J., 1997: A well-calibrated ocean algorithm for Special Sensor Microwave/Imager. *J. Geophys. Res.*, **102**, 8703–8718.

Wentz, F. J., and R. W. Spencer, 1998: SSM/I rain retrievals within a unified all-weather ocean algorithm. *J. Atmos. Sci.*, **55**, 1613–1627.

Wolter, K., and M. S. Timlin, 1993: Monitoring ENSO in COADS with a seasonally adjusted principal component index. *Proc. of the 17th Climate Diagnostics Workshop*, Norman, OK, 52–7, [Available online at http://www.esrl.noaa.gov/psd/enso/mei/WT1.pdf].

Wolter, K., and M. S. Timlin, 1998: Measuring the strength of ENSO events: How does 1997/98 rank? *Weather*, **53**, 315–324.

Wu, X., X.-Z. Liang, and G. J. Zhang, 2003: Seasonal migration of ITCZ precipitation across the equator: Why can't GCMs simulate it? *Geophys. Res. Lett.*, **30**.

Zhang, G. J., and N. A. McFarlane, 1995: Sensitivity of climate simulations to the parameterization of cumulus convection in the Canadian Climate Centre general circulation model. *Atmos. Ocean*, **33**, 407–446.

Zhang, G. J., and M. Mu, 2005: Effects of modifications to the Zhang-McFarlane convection parameterization on the simulation of the tropical precipitation in the National Center for Atmospheric Research Community Climate Model, version 3. *J. Geophys. Res.*, **110**.

Zhou, Y., K.-M. Xu, Y. Sud, and A. Betts, 2011: Recent trends of the tropical hydrological cycle inferred from Global Precipitation Climatology Project and International Satellite Cloud Climatology Project data. *J. Geophys. Res.*, **116**.

Zipser, E. J., 1994: Deep cumulonimbus cloud systems in the tropics with and without lightning. *Mon. Wea. Rev.*, **122**, 1837–1851.

Zipser, E. J., and K. R. Lutz, 1994: The vertical profile of radar reflectivity of convective cells: A strong indicator of storm intensity and lightning probability? *Mon. Wea. Rev.*, **122**, 1751–1759.